Cross-species Comparison Reveals Therapeutic Vulnerabilities Halting Glioblastoma Progression

Leo Carl Foerster[1,2]*, Oguzhan Kaya[1,2]*, Valentin Wüst[2,3], Diana-Patricia Danciu[4], Vuslat Akcay[1,2], Milica Bekavac[1,2], Kevin Chris Ziegler[1], Nina Stinchcombe[1,2], Anna Tang[4], Jocelyn Tang[1], Jan Brunken[1,2], Noelia Gesteira Perez[1], Xiujian Ma[2,5], Ahmed Sadik[6], Christiane Opitz[6], Haikun Liu[5], Christian Rainer Wirtz[7], Anna Marciniak-Czochra[4,8], Simon Anders[3], Angela Goncalves[9], and Ana Martin-Villalba[1†]

[1] Molecular Neurobiology, German Cancer Research Center, 69120 Heidelberg, Germany

[2] Combined Faculty of Mathematics, Engineering and Natural Sciences, University of Heidelberg, 69120 Heidelberg, Germany

[3] BioQuant Centre, University of Heidelberg, 69120 Heidelberg, Germany

[4] Institute of Mathematics, University of Heidelberg, 69120 Heidelberg, Germany

[5] Molecular Neurogenetics, German Cancer Research Center, 69120 Heidelberg, Germany

[6] Metabolic Crosstalk in Cancer, German Cancer Research Center, 69120 Heidelberg, Germany

[7] Department of Neurosurgery, Ulm University Hospital, 89081 Ulm, Germany

[8] Interdisciplinary Center for Scientific Computing, University of Heidelberg, 69120 Heidelberg, Germany

[9] Somatic Evolution and Early Detection, German Cancer Research Center, 69120 Heidelberg, Germany

* These authors contributed equally: Leo Carl Foerster, Oguzhan Kaya

[†] Corresponding author: a.martin-villalba@dkfz-heidelberg.de

Abstract

The growth of a tumor is tightly linked to the distribution of its cells along a continuum of activation states. Here, we systematically decode the activation state architecture (ASA) in a glioblastoma (GBM) patient cohort through comparison to adult murine neural stem cells. Modelling of these data forecast how tumor cells organize to sustain growth and identifies rate of activation as the main predictor of growth. Accordingly, patients with a higher quiescence fraction exhibit improved outcomes. Further, DNA methylation arrays enable ASA-related patient stratification. Comparison of healthy and malignant gene expression dynamics reveals dysregulation of the Wnt-antagonist SFRP1 at the quiescence to activation transition. SFRP1 overexpression renders GBM quiescent and increases overall survival of tumor-bearing mice. Surprisingly, it does so through reprogramming the tumor's stem-like methylome into an astrocyte-like one. Our findings offer a novel patient stratification with clinical impact, new biomarkers and therapeutic avenues to halt GBM progression.

Keywords: Glioblastoma; Adult brain; Astrocytes; Neural stem cells; Quiescence; Activation state; Wnt-signaling; SFRP1; DNA-methylome

Introduction

Glioblastoma (GBM) is the most frequent and lethal adult brain malignancy, with a median survival of only 15 months and limited therapeutic advances in past decades[1]. GBM is particularly life-threatening because the rigid confines of the skull quickly lead to increased intracranial pressure and a high risk of herniation as the tumor grows. As in any cellular system, this growth is sustained by the organization of cells along a continuum of activation states. Like many cancers, GBM growth is fueled by plastic cancer stem cells (CSCs) which give rise to phenotypically diverse tumor cell populations[2,3]. Recent single-cell studies have successfully mapped these diverse transcriptomic profiles to neurodevelopmental cell types[4–10]. Yet, while these neurodevelopmental states are highly plastic and able to regenerate each other[4], their transition dynamics are not fully understood.

In the healthy brain, diverse cellular states are generated by radial glia during development and by neural stem cells (NSCs) in adulthood[11]. While radial glia are mainly found in an active proliferative state during development, in mice, and likely in humans[12], v-SVZ NSCs maintain lifelong neurogenesis through dynamic transitions between distinct activation states[13]. Classically, these activation states include quiescent cells poised to divide, actively proliferating cells that drive immediate expansion, and differentiated cells with specialized functions[14]. Functionally, transitions between these states maintain the NSCs' ability to react to external factors, for example by transiently increasing activation of quiescent NSCs after brain injury[15] or conversely through decreasing their activation rate in aging[15,16]. Thus, different NSC activation state architectures (ASAs) fulfill the organism's needs at various life stages[15,17–19]. GBM cells likewise occupy distinct activation states[10,20–22], and cycling CSCs in particular have been a focus of targeted therapies[5,6,23,24]. However, such approaches are complicated by the intrinsic plasticity of GBM cells which replenish the CSC pool[22], leading to invariable relapse.

There is a critical need to expand therapeutic options for GBM patients in order to achieve more durable treatment outcomes. Treatment with the alkylating agent temozolomide, for example, eliminates cycling cells but spares quiescent tumor cells, which eventually enter cell-cycle and lead to recurrence[25–27]. A similar effect is observed for adult murine NSCs, where temozolomide only suppresses neurogenesis transiently, until quiescent NSCs activate and replenish the stem cell pool[15]. Here, comparing GBM to NSCs is instructive, revealing Wnt signaling as an essential regulator of activation state[15,28] which can trigger relevant tumor phenotypes[29]. Additional principles governing CSCs may also be gleamed from healthy stem cells. Recent studies show that astrocytes may acquire stemness following injury[30,31], transitioning from a dormant (ie. long-term quiescent) to an NSC-like state by switching from a characteristic astrocytic to an NSC methylome[32]. Although several studies have characterized GBM methylation at single-cell resolution[21,33], it remains unclear whether GBM cells mimic the methylation remodeling found in healthy v-SVZ populations. Overall, improved understanding of the ASAs that sustain GBM growth may reveal novel therapeutic strategies[34]. Indeed, GBMs are notorious for their plasticity of CSC fates[22,35], likely manifesting in diverse tumor ASAs, each of which may benefit from distinct therapeutic strategies.

In this work, we decode the individual ASA for each GBM patient by aligning single GBM cell transcriptome with a reference NSC ASA of the adult murine brain through a dedicated tool,

ptAlign. These unique ASAs are integrated into mathematical models to explain GBM population dynamics and identify parameters influencing tumor growth. Using ptAlign, we compare inter-tumor gene expression dynamics in 51 GBMs to the healthy counterpart, identifying the secreted Wnt antagonist SFRP1 as recurrently dysregulated. Reintroducing SFRP1 stalls tumor growth *in vivo* and reprograms the tumor from a NSC-like into an astrocyte-like methylome, significantly improving overall survival of GBM-bearing mice. Our approach establishes a framework for the inference of comparative tumor hierarchies, enabling patient stratification and target discovery.

Results

Activation State Architectures in the Fetal and Adult Mammalian Brain

During brain development, neural progenitor cells are committed to generating differentiated progeny and are eliminated upon completion of their developmental role. In contrast, adult somatic stem cells are maintained to ensure lifelong tissue homeostasis through continuous progeny generation, analogous to cancer stem cells, which persist to support ongoing tumor growth. To enable a reference-based prediction of GBM activation state architecture (ASA), we leverage their similarity to healthy NSCs. Ideally, we would reference adult human NSC lineages, as these serve as a model for how tumor cells might organize and differentiate within a similar environment. However, datasets capturing adult human neurogenesis remain largely unavailable[28,36–38]. Instead, we turn to the adult mouse v-SVZ, a region that harbors quiescent NSCs which populate a lineage of quiescent and active states and ultimately give rise to different neural cell types[11,15,39] (Fig. 1a). scRNA-seq provides a snapshot of the v-SVZ NSC pool, allowing ASA and state transitions to be decoded by pseudotime analysis. We compiled a 14,793-cell murine v-SVZ NSC lineage dataset[15,19,40] and fit a NSC-to-neuron differentiation trajectory by diffusion pseudotime (Fig. S1a-b). In this trajectory, we delineated distinct activation states including quiescence (Q), activation (A), and differentiation (D); collectively referred to as QAD (Fig. 1b; Fig. S1c). This approach places v-SVZ astrocytes at the lineage onset, supported by their transcriptional similarity to NSCs and their latent neurogenic potential[32]. The QAD stages in the NSC ASA are identifiable from pseudotime alone, and we derived a 242-gene pseudotime-predictive gene set (SVZ-QAD: Methods; Fig. S1d; Table S2) to facilitate their comparison across species.

To contrast ASAs in fetal and adult neurogenesis against GBM and include the healthy human context, we examined over 600,000 single-cell transcriptomes from human cortical development[41]. These cells exhibited a similar lineage progression to adult NSCs, and mapping QAD-stage frequencies over developmental time revealed a low prevalence of quiescent cells that increased in late development but did not surpass 5% (Fig. 1c; Fig. S1e). A similar lineage and low incidence of quiescent cells was found in human brain organoids (HBOs) which mimic cortical development[42] (Fig. S1f-h). Thus, although fetal and adult neurogenesis share a similar progression, the adult brain ASA is characterized by a significantly increased abundance of Q-stage cells.

We further analyzed QAD-stages in 399 bulk GBM samples from TCGA[43] and Wu et al[24]. Patients in this cohort had an average age at diagnosis of 59 (Fig. 1d), underscoring the late emergence of these tumors within the adult brain[1]. We found Q-stage gene expression enriched among GBMs

(Fig. 1e), consistent with the increased abundance of quiescence in the adult NSC ASA. Single-cell profiling of a GBM patient derived orthotopic xenograft (PDX, pseudonymously T6) supported this finding, identifying a tumor ASA with substantial Q-stage expression (Fig. 1f) within a UMAP structure closely resembling the adult v-SVZ NSC lineage (Fig. 1b). We identified distinct cell morphologies in this tumor (Fig. 1F and S2). Characteristics of the T6 GBM were replicated in cells implanted into the fetal context of HBOs (henceforth as patient derived allografts, PDAs; Fig. S2). Finally, comparing QAD-stage frequencies in the T6 PDX with young and old adult v-SVZ populations and late cortical development revealed the greatest similarity in ASA between GBM and the aged v-SVZ NSC lineage (Fig. 1g). We conclude that referencing fetal development to decode the ASA of GBM fail to capture relevant aspects of tumor biology due to the lack of a quiescent state. Instead, adult NSC lineages provide a more accurate framework, motivating a comparative view of GBM organization grounded in adult v-SVZ NSC QAD-ASA.

ASAs Inferred by ptalign

Having established parallels between GBMs and the adult v-SVZ NSC lineage, we sought to systematically resolve the distinct patient's ASAs through the lens of healthy lineage dynamics with a computational tool that we termed pseudotime alignment, ptalign. This tool maps tumor cells onto a reference lineage trajectory (here the murine v-SVZ NSC lineage), thereby resolving both individual cell stages and the transitions between them (Fig. 2a). A pseudotime-similarity metric derived from gene expression correlations between a query cell and regularly sampled increments along the reference pseudotime underlies this mapping (Fig. 2b). Because cellular differentiation is governed by gradual transcriptional changes, each cell's pseudotime-similarity profile serves as a signature of its position in pseudotime. By normalizing these profiles and focusing on their shape, a neural network is able to learn an efficient mapping between cellular similarity profiles and pseudotimes (Fig. 2c). For training, we use similarity profiles of the pseudotime-masked reference, which serve as a convenient ground truth. Cycling cells are excluded to limit inference to non-branching pseudotimes. The trained network then predicts 'aligned' pseudotimes for query (tumor) cells from their pseudotime-similarity profiles (Fig. 2d), applying additional heuristics to exclude out-of-distribution cells. The tumor ASA is finally determined by thresholding in the aligned pseudotime, as v-SVZ QAD-stages are identifiable from pseudotime alone. Applied to the T6 GBM, ptalign reported an adult-like ASA consistent with gene-set scoring, revealing a hierarchy of cells transitioning all activation states (Fig. 2a, right panel).

The approach outlined in ptalign provides several key innovations over existing trajectory alignment algorithms. Unlike traditional dynamic programming-based approaches that require two samples with known pseudotimes and produce a third, shared pseudotime[44–47], ptalign takes one or more scRNA-seq tumor samples, a reference scRNA-seq dataset, and a pseudotime-predictive gene set to yield a single, reference-based tumor pseudotime. By aligning all tumor cells along a common differentiation axis, ptalign ensures that cells at the same pseudotime exhibit comparable transcriptomic profiles across different tumors, facilitating systematic tumor-tumor and tumor-healthy comparisons. This strategy also enables the transfer of contextual information from healthy lineage trajectories, providing important insights for the discovery of specific tumor vulnerabilities.

To validate ptalign performance, we assessed its ability to reconstruct underlying dynamics across several benchmarking scenarios. First, applying ptalign to reconstruct neurogenic lineages in our HBO dataset (Fig. S1h) and an independent v-SVZ NSC lineage dataset showed strong correlations between ptalign-derived and dataset-derived pseudotimes (v-SVZ Pearson=0.95; HBO Pearson=0.85; Fig. S3a-f). In ptalign, both the reference and aligned pseudotimes capture the same underlying process, motivating their comparison by dynamic time warping[48] (DTW). As a successful alignment matches query cells with the reference trajectory at each point in pseudotime, we can expect a characteristic narrow and highly correlated diagonal in the DTW matrix. We quantify the shape of this diagonal by a score-maximizing traceback which is compared across gene-permuted ptalign runs to derive a p-value representing the statistical confidence in aligned pseudotimes (Fig. 2e; Fig. S3g; Methods). Applying ptalign to 55 primary GBM scRNA-seq datasets (see below) and other tissue cancers[49] revealed QAD dynamics detected in 51/55 GBMs, but not in other cancers ($p<0.05$; Fig. S3h), highlighting the sensitivity of this permutation approach. We further benchmarked ptalign against established trajectory inference methods, demonstrating comparable or better ability to reconstruct coherent trajectories (Fig. S3i-j; Methods). Comparing a dataset of healthy and diseased lung analyzed in Genes2Genes[47], ptalign not only recovered the previously reported aberrant gene dynamics, but also highlighted the involvement of TNF-alpha aberrancies in this disease[50] (Fig. S3k-o; Methods). Taken together, these benchmarks demonstrate the robust and scalable framework provided by ptalign to enable ASA prediction and the comparative analysis of gene expression dynamics in healthy and disease contexts.

ASA Informs Tumor Growth Dynamics, Prognosis and Patient Stratification

To interrogate inter-tumoral heterogeneity in GBM, we compiled 55 primary GBM scRNA-seq datasets[4,6,8,51–55] for which we determined v-SVZ-aligned pseudotimes and ASAs (Table S1; Methods). 51 GBMs passed the v-SVZ ptalign permutation threshold ($p<0.05$), and conventional UMAP clustering resolved these tumors by patient origin, obscuring underlying biological similarities (Fig. 2f-g). Instead, projecting these tumors onto a common cell trajectory using ptalign revealed a landscape of GBM ASA comprised of heterogeneous Q- and D-dominated tumors (Fig. 2h). Although clinical metadata were limited in this cohort, we found a significant association between ASA and patient age as well as IDH-mutation status, while no clear association was detected for other features including clonal architecture[5], tumor location, or MGMT methylation status[56] (ANOVA $p<0.05$; Fig. S4 and S5).

Next, we addressed the potential prognostic value of the decoded tumor ASAs. By integrating these data into mathematical models, we can forecast how a tumor evolves, when it might surge in growth, and how it could respond to treatment. As *in vivo* models of GBM hierarchy support an adult NSC-like organization rooted in a quiescent progenitor[10,20,57], we applied a system of ordinary differential equations (ODEs) adapted from established models of v-SVZ population dynamics[19,58] to model tumor progression (Fig. 3a; Data S1). Fitting this model to our 51-GBM cohort, we simulated QAD population dynamics, faithfully recapitulating tumor-specific ASAs and generating quantitative estimates of tumor growth rates. This revealed a positive correlation between growth rate and the proportion of A-stage cells which was reversed for Q-stage cells (Fig. 3b). Notably, our simulated QAD-stage proportions for all 51 GBMs rapidly reached

equilibrium during early tumor development (Fig. 3c), reflecting the early establishment of growth-supporting architectures. To gain insights into the processes governing the underlying tumor ASA, we investigated the effect of our modeled parameters on tumor growth rates. The activation rate (i.e. Q-A transition, representing the exit of quiescence) was the strongest predictor of tumor growth rate (59.7% explained), while a subset of tumors compensated for lower activation rates through increased self-renewal (Fig. 3d-e). This is consistent with adult NSCs, where decreasing activating rates in older ages are compensated through increased self-renewal in an interferon-dependent manner[19]. In sum, we find that Q-A transitions are a critical determinant of tumor growth and progression. We further decomposed 399 primary human GBMs using a 271-gene GBM-QAD signature (Methods; Table S2), revealing Q-scores significantly associated with improved patient outcomes (multivariate Cox p=0.035; Fig. 3f and Fig. S6a-b). These insights highlight the role of Q-stage cells in sustaining GBM growth[25,27,57] and pinpoint the Q-A transition as a promising target for therapeutic intervention.

Collectively, our results reveal that tumor ASA has prognostic significance and informs parameters related to tumor growth, thereby guiding the identification of therapeutic targets. Consequently, developing clinical biomarkers for patient stratification based on GBM ASAs is a clear priority. Thus, we examined whether a patient's methylation profile correlates with their ASA, since QAD-stages of the v-SVZ NSC lineage display distinct methylomes[32] and such profiling is already employed in the WHO-classification of brain tumors[59]. Analysis of 83 IDH-wildtype tumors with matched RNA and methylation profiles revealed that a PCA of methylation data decomposed tumors according to their dominant RNA-defined QAD-stage (Fig. 3g, Table S6). We found that inter-tumoral RNA- and methylation-distances were correlated, motivating us to train an ElasticNet model to predict RNA scores from tumor methylomes (Fig. S6c; Methods). These predictions achieved a mean Pearson correlation of 0.70 on holdout samples (Fig. 3h), demonstrating that GBM ASA can be inferred from bulk methylomes. We realize this approach below, leveraging comparative pseudotime expression dynamics to derive salient biomarkers. Taken together, our modeling and biomarker analyses reveal the central role of Q-stage cells and the Q-A transition in shaping patient outcomes, motivating methylation-based biomarkers for patient stratification by ASA.

Target Discovery by Comparative Analysis of Dysregulated Expression Dynamics

By projecting tumor cells onto a shared reference trajectory using ptalign, we enable direct comparisons of healthy versus malignant expression dynamics. Current approaches for detecting differential gene expression along pseudotime are chiefly sensitive to differences in expression levels, which are frequently altered in tumors and can overshadow changes in the underlying expression dynamics. To overcome this limitation, we normalize the area under pseudotime expression curves and apply the Earth Mover's Distance[60] (EMD) to quantify differences in curve shape that represent differential regulation along the underlying trajectory. This way, genes with similar dynamics obtain lower EMD scores while those with divergent expression patterns obtain high EMD scores (Fig. 4a). We use this approach to identify putative biomarkers, characterized by consistent expression dynamics and changes in overall expression, as well as therapeutic targets, which exhibit consistently altered expression dynamics.

To explore actionable biomarkers for patient stratification, we computed pairwise EMDs for two groups of Q- and D-dominated GBMs (Fig. S6d-e; Table S3). This analysis highlighted SOX11 and STMN1 as potential biomarkers with consistent expression dynamics independent of ASA, which also exhibited group-specific expression levels and methylation patterns (Fig. S6f-g). In contrast, genes including KLF4 and ZFP36 exhibited differential expression dynamics by group that were not consistently echoed by their group-specific expression levels (Fig. S6h-i), thus undermining their prognostic value and instead being relevant predictors of the tumor biology.

We next compared EMD values between GBMs and the v-SVZ reference to identify genes with consistently aberrant dynamics which could serve as therapeutic targets. This required pre-selection of genes universally expressed in both healthy and malignant contexts, revealing 169 genes with consistently dysregulated expression dynamics in GBM (Fig. 4b; Table S3; Methods). These genes enriched in processes commonly disrupted in GBM, including cell-cell adhesion, neuronal differentiation, angiogenesis, and Wnt signaling[22] (Fig. 4c). Indeed, Wnt pathway genes outnumbered those from BMP, Notch, or SHH signaling pathways among our GBM dysregulated genes (Fig. 4d). These Wnt genes in turn showed enriched Q-stage expression in the v-SVZ lineage (Fig. 4e). Among these, SFRP1 was one of the most consistently dysregulated genes, notably peaking at the Q-A transition in v-SVZ NSCs (Fig. 4f-g). Thus, SFRP1 and other genes may contribute to aberrant Wnt dynamics at the Q-A transition, contributing to GBM progression.

To further investigate the role of dysregulated Wnt signaling in GBMs, we measured canonical Wnt (cWnt) activity levels across QAD-stages in both healthy and tumor lineages using genetic reporters (TCF/Lef-EGFP; Methods) (Fig. 5a). Analysis of the v-SVZ NSCs lineage in this cWnt reporter line revealed a tight regulation of Wnt activity across QAD-stages: cWnt was highest at the Q-stage, decreased in the A-stage, and resurged in the D-stage (Fig. 5b-c; Fig. S7a). In contrast, GBM cells exhibited sustained cWnt-reporter activity across all QAD stages (Fig. 5b). This was confirmed by spatial transcriptomics of a cWnt-reporter PDX, revealing consistent cWnt activity across brain regions (Table S4; Fig. 5d-e; Fig. S7b-d) with one notable exception: ventricular outgrowths (Fig. 5f). Notably, these outgrowths as well as *in vitro* cultured GBM spheroids lack cWnt activity (Fig. S7e-h), possibly due to their lack of contact with brain parenchyma[61]. Intriguingly, ventricular outgrowths were characterized by A- and D-stage cells organized along distinct gradients with Q cells lying at the ventricular wall (Fig. S7i). Overall, our comparative approach reveals that GBMs lose the tight regulation of cWnt signaling that accompanies the exit from quiescence in healthy NSCs, prompting further investigation of dysregulated factors involved in this transition.

SFRP1-induced Quiescence Stalls Tumor Growth

Using ptalign, we identified SFRP1, a secreted Wnt antagonist[28], as one of the most consistently dysregulated genes in GBM (Fig. 4f). Thus, to disrupt tumor ASA by modulating cWnt signaling at the Q-A transition, we cloned SFRP1 downstream of the TCF/Lef-promoter in T6 GBM (Fig. 6a; Fig. S8a-b; Methods). Strikingly, SFRP1-overexpression (OE) in tumor cells significantly improved overall survival in mouse PDXs, while scRNA-seq revealed that GBM cells were stalled in a quiescent astrocyte-like stage (Fig. 6b-d). Applying our GBM population models revealed that the stark reduction in tumor growth rate resulted from a decrease in activation rate (Fig. 6e),

pinpointing the action of SFRP1 to the Q-A transition. These results were mirrored by the overexpression of NOTUM, another recurrently dysregulated cWnt antagonist[62] expressed at the Q-A transition (Fig. S8c-e). NOTUM-OE and SFRP1-OE tumors exhibited similar transcriptional profiles (Fig. S8f; Pearson=0.76), suggesting these converged on a set of overlapping downstream effectors.

The astrocytic shift of SFRP1-OE transcriptomes was accompanied by a dramatic morphological transformation from a neuron-like appearance in GBM cells homing to the cortex to the star-shaped form typical of astrocytes (Fig. 6f). We further employed spatial transcriptomics to explore the distribution of QAD-stage cells in SFRP1-OE tumors. We found most tumor cells confined to the Q-stage across all brain regions (Fig. 6g), while neighborhood enrichment highlighted their preference for neuronal proximity (Fig. S8g). The only exception was found in SFRP1-OE ventricular outgrowths, which organized along A-D gradients (Fig. S8h) as previously, as the lack of cWnt activity impairs the action of SFRP1. This finding also underscores the limited range of secreted Wnt factors[63]. Indeed, while tumor cells exhibited increased quiescence in a SFRP1-OE PDA model, healthy cell transcriptomes remained unperturbed (Fig. S8i-k).

In a recent study, we demonstrated that two functionally distinct cells, dormant v-SVZ NSCs and astrocytes, exhibit similar transcriptomes but differ in their DNA-methylome[32]. Notably, an ischemic injury to the brain remodels the astrocyte-methylome into a NSC-like one and thereby inducing stemness. As SFRP1-OE in GBM cells induced an astrocyte morphology and functional quiescence, we asked to what extent this methylome remodeling is conserved across species and disease contexts. We analyzed our previously reported v-SVZ variably methylated regions[32] (VMRs) in three technical replicates of SFRP1-OE and control PDX tumors (Fig. 7a). Analysis of v-SVZ VMRs at their syntenic human coordinates (Methods; Table S6) revealed preferential hypomethylation of astrocyte-specific VMRs in SFRP1-OE tumor cells (Fig. 7b; $p<0.001$), confirming that SFRP1-OE rewires tumor cell methylomes along with their transcriptomes and morphology. Notably, one of the most divergently methylated VMRs overlapped an NFIB-promotor (Fig. 7c): its product, NFIB, is the primary transcriptional activator of the astrocyte marker GFAP[64] and is also used to reprogram iPSCs into astrocytes[65]. Consistently, we identified a significant increase in NFIB and GFAP transcript-expressing cells in SFRP1-OE tumors (Fig. 7d). As methylation generally acts to restrict cellular plasticity[66], the significant degree of conserved remodeling in SFRP1-OE tumor astrocytes might render them refractory to subsequent reactivation (Fig. 7e). Collectively, our findings demonstrate the unique advantages of decoding ASA in solid tumors to enable target identification and effectively disrupt tumor growth.

Discussion

Tumors retain characteristics of their tissue-of-origin[67], forming hierarchies that mirror developmental lineage maps[68]. Here, we leveraged the similarities between GBMs and adult NSCs by systematically comparing malignant hierarchies to healthy stem cell lineages to decode ASAs that fuel tumor growth. To achieve this, we developed ptalign, a computational method that aligns tumor cells within a reference pseudotime to inform activation states. By aligning tumors onto a single reference, ptalign enables robust inter-tumor comparisons which guide patient stratification and open up the potential for personalized therapeutic approaches.

Central to our findings is the ability for ptalign to identify cells transitioning between activation states, representing critical bottlenecks for therapeutic intervention. This is achieved through a reference-based approach, which maps tumor cells within a healthy lineage trajectory, enabling the transfer of contextual knowledge and simultaneous comparison of tumors with both other tumors and healthy populations. This approach builds on a growing appreciation for the conserved development of tumor hierarchies along a healthy template[68], positioning ptalign as a versatile tool for dissecting tumor organization across malignancies. Although ptalign currently supports only non-branching trajectories, emerging methods tackling branched alignments[78] and DTW[79] could extend its applicability.

By assessing activation states in bulk and single-cell GBMs, alongside transcriptomic and DNA methylation-contexts, we gained insights into the ASAs that support tumor growth. Quiescence was a ubiquitous feature of GBM ASAs, with most tumors more closely aligned to adult than fetal NSC ASAs. While both fetal and adult NSC populations exhibit a similar diversity of cellular fates, quiescence is largely absent during fetal development[11]. Using mathematical models of GBM population dynamics, we identified the Q-A transition as central to tumor growth. This aligns with *in vivo* studies of GBM that report a tumor hierarchy rooted in a quiescent progenitor[10,20,57]. However this organization is challenged *in vitro*[35,69], possibly due to the growth-factor-enriched conditions that lead to a fetal ASA, limiting their ability to capture quiescent cell dynamics. Despite these differences, the activation of therapy-resistant quiescent cells to repopulate the tumor[25,26] underscores the clinical relevance of this state as well as the need to device strategies disrupting the Q-A transition. Importantly, linear ODE models of cell population dynamics capture average behaviour at the population level, smoothing out individual cell variability. While single-cell trajectories may be non-linear, these models abstract away such complexity to describe aggregate trends.

NSCs exhibit an increasing quiescence-bias with age that correlates with increased expression of SFRP5[15,16]. Mathematical modeling identified a reduced rate of activation, that increases upon SFRP5 neutralization[15]. In contrast, our mathematical modeling of GBM shows an elevated activation rate, which can be suppressed by overexpressing SFRP1. These models also suggest that while GBM growth in most patients is driven by changes in activation rate, a subset of tumors with very low activation rates maintain growth through self-renewal—a mechanism similarly observed in the aging healthy brain upon deletion of interferon receptors[19]. Further studies are thus needed to explore signaling pathways regulating compensation through self-renewal. SFRP1 overexpression may be particularly beneficial for recurrent GBMs, which are more aggressive and exhibit a proneural shift[70].

Through ptalign-driven comparisons, we identified pervasive dysregulation of cWnt pathway genes in GBM. The dysregulated Wnt antagonists SFRP1 and NOTUM were found at the Q-A transition and independent overexpression of either of them induced a pronounced astrocytic shift in tumor cell morphology, transcriptome, and methylome. The resulting methylome changes mirrored remodeling observed in murine brain regeneration, where parenchymal astrocytes undergo a switch to an NSC-like state following ischemic injury[32]. This convergence of methylome remodeling between murine regeneration and human GBM suggests that conserved epigenetic mechanisms may also underlie human brain regeneration. These findings underscore the reciprocal developmental parallels between healthy and malignant tissues, advancing a comparative framework that informs both tumor biology as well as fundamental processes regulating healthy cells. Because methylation constrains cellular plasticity by restricting the genome to the specific functions of terminally differentiated cells[66], future work will determine whether SFRP1-mediated methylome remodeling enduringly locks GBM cells in a quiescent state, offering a potential therapeutic avenue. This contrasts with the transient increase in quiescence observed following chemotherapy- or radiotherapy-induced depletion of the active tumor population[25,26], which ultimately leads to aggressive tumor recurrence.

The quiescent phenotype observed in SFRP1-OE tumor cells is consistent with its role in healthy NSCs, where knockdown of SFRP1 increased activation at the cost of depletion of the quiescent NSC pool[28]. Crucially, our strategy in SFRP1-OE targets a transition over a stage, enabling an effective disruption of tumor dynamics. SFRP1 effectively synchronized the entire tumor population in a Q-stage, notably without perturbing healthy cells, paving the way for combination therapies that complement existing treatments to improve patient outcomes.

Few molecular biomarkers reliably predict GBM therapy outcomes[56], though methylation has proved a robust and cost-effective means for tumor classification[59,71]. We identified cellular activation states encoded in tumor methylomes which we used to predict ASA signatures from bulk samples. However, while SFRP1-OE methylome remodeling was found in WGBS it was not detectable on commercial methylation microarrays owing to their limited CpG coverage, mainly featuring promoter regions that do not inform on stem cell trajectories[32]. We additionally demonstrated that biomarker efficacy can be compromised by stage-specific expression dynamics, and identified SOX11 and STMN1 as potential markers with stable expression dynamics that provide transcriptome and methylation-based means to identify eg. those patients which are likely to benefit from SFRP1 therapy. Of note, the EMD-based approach that identified these markers in Q- vs D-biased GBMs extends to any two patient groups, motivating the development of tailored interventions.

Our GBM PDXs revealed that ventricular outgrowths consistently lacked Wnt activity and harbored large numbers of active, cycling cells, aligning with the aggressive clinical course observed in patients with ventricular tumors[72]. Wnt activity in tumor cells may depend on interactions with the surrounding brain parenchyma[61], potentially through synaptic neuron-tumor networks[73]. Likewise, the cerebrospinal fluid, which contacts the ventricles and contains SHH ligands known to antagonize Wnt signaling[74,75], may drive the increased activation observed in ventricular outgrowths[76]. Notably, the absence of quiescent cells in these outgrowths mirrors the behavior of metastatic cells at the vessel lumen, where cWnt activity is only gained upon

extravasation and triggers a proliferative-to-dormant switch[77]. These findings underscore the critical influence the microenvironment has on shaping tumor phenotypes[22].

Overall, our study provides a systematic framework for patient stratification and therapeutic target identification, emphasizing the importance of targeting dynamic tumor processes to disrupt tumor progression.

References

1. Tan, A. C. *et al.* Management of glioblastoma: State of the art and future directions. *CA A Cancer J Clinicians* **70**, 299–312 (2020).

2. Gimple, R. C., Yang, K., Halbert, M. E., Agnihotri, S. & Rich, J. N. Brain cancer stem cells: resilience through adaptive plasticity and hierarchical heterogeneity. *Nat Rev Cancer* **22**, 497–514 (2022).

3. Pérez-González, A., Bévant, K. & Blanpain, C. Cancer cell plasticity during tumor progression, metastasis and response to therapy. *Nat Cancer* **4**, 1063–1082 (2023).

4. Neftel, C. *et al.* An Integrative Model of Cellular States, Plasticity, and Genetics for Glioblastoma. *Cell* **178**, 835-849.e21 (2019).

5. Bhaduri, A. *et al.* Outer Radial Glia-like Cancer Stem Cells Contribute to Heterogeneity of Glioblastoma. *Cell Stem Cell* **26**, 48-63.e6 (2020).

6. Couturier, C. P. *et al.* Single-cell RNA-seq reveals that glioblastoma recapitulates a normal neurodevelopmental hierarchy. *Nat Commun* **11**, 3406 (2020).

7. Castellan, M. *et al.* Single-cell analyses reveal YAP/TAZ as regulators of stemness and cell plasticity in glioblastoma. *Nat Cancer* **2**, 174–188 (2020).

8. Richards, L. M. *et al.* Gradient of Developmental and Injury Response transcriptional states defines functional vulnerabilities underpinning glioblastoma heterogeneity. *Nat Cancer* **2**, 157–173 (2021).

9. Sojka, C. *et al.* Mapping the developmental trajectory of human astrocytes reveals divergence in glioblastoma. *Nat Cell Biol* (2025) doi:10.1038/s41556-024-01583-9.

10. Hamed, A. A. *et al.* Gliomagenesis mimics an injury response orchestrated by neural crest-like cells. *Nature* (2025) doi:10.1038/s41586-024-08356-2.

11. Kriegstein, A. & Alvarez-Buylla, A. The Glial Nature of Embryonic and Adult Neural Stem Cells. *Annu. Rev. Neurosci.* **32**, 149–184 (2009).

12. Ernst, A. *et al.* Neurogenesis in the Striatum of the Adult Human Brain. *Cell* **156**, 1072–1083 (2014).

13. Obernier, K. & Alvarez-Buylla, A. Neural stem cells: origin, heterogeneity and regulation in the adult mammalian brain. *Development* **146**, dev156059 (2019).

14. Beumer, J. & Clevers, H. Hallmarks of stemness in mammalian tissues. *Cell Stem Cell* **31**, 7–24 (2024).

15. Kalamakis, G. *et al.* Quiescence Modulates Stem Cell Maintenance and Regenerative Capacity in the Aging Brain. *Cell* **176**, 1407-1419.e14 (2019).

16. Bast, L. *et al.* Increasing Neural Stem Cell Division Asymmetry and Quiescence Are Predicted to Contribute to the Age-Related Decline in Neurogenesis. *Cell Reports* **25**, 3231-3240.e8 (2018).

17. Basak, O. *et al.* Troy+ brain stem cells cycle through quiescence and regulate their number by sensing niche occupancy. *Proc. Natl. Acad. Sci. U.S.A.* **115**, (2018).

18. Harris, L. *et al.* Coordinated changes in cellular behavior ensure the lifelong maintenance of the hippocampal stem cell population. *Cell Stem Cell* **28**, 863-876.e6 (2021).

19. Carvajal Ibañez, D. *et al.* Interferon regulates neural stem cell function at all ages by orchestrating mTOR and cell cycle. *EMBO Mol Med* **15**, e16434 (2023).

20. Lan, X. *et al.* Fate mapping of human glioblastoma reveals an invariant stem cell hierarchy. *Nature* **549**, 227–232 (2017).

21. Chaligne, R. *et al.* Epigenetic encoding, heritability and plasticity of glioma transcriptional cell states. *Nat Genet* **53**, 1469–1479 (2021).

22. Prager, B. C., Bhargava, S., Mahadev, V., Hubert, C. G. & Rich, J. N. Glioblastoma Stem Cells: Driving Resilience through Chaos. *Trends in Cancer* **6**, 223–235 (2020).

23. Singh, S. K. *et al.* Identification of human brain tumour initiating cells. *Nature* **432**, 396–401 (2004).

24. Wu, Y. *et al.* Glioblastoma epigenome profiling identifies SOX10 as a master regulator of molecular tumour subtype. *Nat Commun* **11**, 6434 (2020).

25. Xie, X. P. *et al.* Quiescent human glioblastoma cancer stem cells drive tumor initiation, expansion, and recurrence following chemotherapy. *Developmental Cell* **57**, 32-46.e8 (2022).

26. Chen, J. *et al.* A restricted cell population propagates glioblastoma growth after chemotherapy. *Nature* **488**, 522–526 (2012).

27. Sabelström, H. *et al.* High density is a property of slow-cycling and treatment-resistant human glioblastoma cells. *Experimental Cell Research* **378**, 76–86 (2019).

28. Donega, V. *et al.* Single-cell profiling of human subventricular zone progenitors identifies SFRP1 as a target to re-activate progenitors. *Nat Commun* **13**, 1036 (2022).

29. Lee, Y., Lee, J.-K., Ahn, S. H., Lee, J. & Nam, D.-H. WNT signaling in glioblastoma and therapeutic opportunities. *Laboratory Investigation* **96**, 137–150 (2016).

30. Magnusson, J. P. *et al.* A latent neurogenic program in astrocytes regulated by Notch signaling in the mouse. *Science* **346**, 237–241 (2014).

31. Duan, C. *et al.* Striatal astrocytes transdifferentiate into functional mature neurons following ischemic brain injury. *Glia* **63**, 1660–1670 (2015).

32. Kremer, L. P. M. *et al.* DNA methylation controls stemness of astrocytes in health and ischaemia. *Nature* **634**, 415–423 (2024).

33. Johnson, K. C. *et al.* Single-cell multimodal glioma analyses identify epigenetic regulators of cellular plasticity and environmental stress response. *Nat Genet* **53**, 1456–1468 (2021).

34. Suvà, M. L. & Tirosh, I. The Glioma Stem Cell Model in the Era of Single-Cell Genomics. *Cancer Cell* **37**, 630–636 (2020).

35. Dirkse, A. *et al.* Stem cell-associated heterogeneity in Glioblastoma results from intrinsic tumor plasticity shaped by the microenvironment. *Nat Commun* **10**, 1787 (2019).

36. Couturier, C. P. *et al.* Glioblastoma scRNA-seq shows treatment-induced, immune-dependent increase in mesenchymal cancer cells and structural variants in distal neural stem cells. *Neuro-Oncology* **24**, 1494–1508 (2022).

37. Siletti, K. *et al.* Transcriptomic diversity of cell types across the adult human brain. *Science* **382**, eadd7046 (2023).

38. Chen, X. *et al.* A brain cell atlas integrating single-cell transcriptomes across human brain regions. *Nat Med* **30**, 2679–2691 (2024).

39. Llorens-Bobadilla, E. *et al.* Single-Cell Transcriptomics Reveals a Population of Dormant Neural Stem Cells that Become Activated upon Brain Injury. *Cell Stem Cell* **17**, 329–340 (2015).

40. Kremer, L. P. M. *et al.* High throughput screening of novel AAV capsids identifies variants for transduction of adult NSCs within the subventricular zone. *Molecular Therapy - Methods & Clinical Development* **23**, 33–50 (2021).

41. Nano, P. R. *et al.* A Meta-Atlas of the Developing Human Cortex Identifies Modules Driving Cell Subtype Specification. Preprint at https://doi.org/10.1101/2023.09.12.557406 (2023).

42. Lancaster, M. A. & Knoblich, J. A. Generation of cerebral organoids from human pluripotent stem cells. *Nat Protoc* **9**, 2329–2340 (2014).

43. Liu, J. *et al.* An Integrated TCGA Pan-Cancer Clinical Data Resource to Drive High-Quality Survival Outcome Analytics. *Cell* **173**, 400-416.e11 (2018).

44. Alpert, A., Moore, L. S., Dubovik, T. & Shen-Orr, S. S. Alignment of single-cell trajectories to compare cellular expression dynamics. *Nat Methods* **15**, 267–270 (2018).

45. Alpert, A. *et al.* Alignment of single-cell trajectories by tuMap enables high-resolution quantitative comparison of cancer samples. *Cell Systems* **13**, 71-82.e8 (2022).

46. Laidlaw, R. F., Briggs, E. M., Matthews, K. R., McCulloch, R. & Otto, T. D. TrAGEDy: Trajectory Alignment of Gene Expression Dynamics. Preprint at https://doi.org/10.1101/2022.12.21.521424 (2022).

47. Sumanaweera, D. *et al.* Gene-level alignment of single-cell trajectories. *Nat Methods* **22**, 68–81 (2025).

48. Aach, J. & Church, G. M. Aligning gene expression time series with time warping algorithms. *Bioinformatics* **17**, 495–508 (2001).

49. Gavish, A. *et al.* Hallmarks of transcriptional intratumour heterogeneity across a thousand tumours. *Nature* **618**, 598–606 (2023).

50. Piguet, P. F., Ribaux, C., Karpuz, V., Grau, G. E. & Kapanci, Y. Expression and Localization of Tumor Necrosis Factor-a and Its mRNA in Idiopathic Pulmonary Fibrosis. **143**, (1993).

51. Jacob, F. *et al.* A Patient-Derived Glioblastoma Organoid Model and Biobank Recapitulates Inter- and Intra-tumoral Heterogeneity. *Cell* **180**, 188-204.e22 (2020).

52. Yuan, J. *et al.* Single-cell transcriptome analysis of lineage diversity in high-grade glioma. *Genome Med* **10**, 57 (2018).

53. Wang, L. *et al.* The Phenotypes of Proliferating Glioblastoma Cells Reside on a Single Axis of Variation. *Cancer Discovery* **9**, 1708–1719 (2019).

54. Wang, R. *et al.* Adult Human Glioblastomas Harbor Radial Glia-like Cells. *Stem Cell Reports* **14**, 338–350 (2020).

55. Chen, A. X. *et al.* Single-cell characterization of macrophages in glioblastoma reveals MARCO as a mesenchymal pro-tumor marker. *Genome Med* **13**, 88 (2021).

56. Śledzińska, P., Bebyn, M. G., Furtak, J., Kowalewski, J. & Lewandowska, M. A. Prognostic and Predictive Biomarkers in Gliomas. *IJMS* **22**, 10373 (2021).

57. Muskovic, W. *et al.* Adult-type diffuse gliomas share recurring cell states driven by a common astrocyte-like glioma stem cell population. Preprint at https://doi.org/10.1101/2024.06.13.598923 (2024).

58. Danciu, D.-P., Hooli, J., Martin-Villalba, A. & Marciniak-Czochra, A. Mathematics of neural stem cells: Linking data and processes. *Cells & Development* **174**, 203849 (2023).

59. Louis, D. N. *et al.* The 2021 WHO Classification of Tumors of the Central Nervous System: a summary. *Neuro-Oncology* **23**, 1231–1251 (2021).

60. Rubner, Y., Tomasi, C. & Guibas, L. J. The Earth Mover's Distance as a Metric for Image Retrieval.

61. Portela, M. *et al.* Glioblastoma cells vampirize WNT from neurons and trigger a JNK/MMP signaling loop that enhances glioblastoma progression and neurodegeneration. *PLoS Biol* **17**, e3000545 (2019).

62. Kakugawa, S. *et al.* Notum deacylates Wnt proteins to suppress signalling activity. *Nature* **519**, 187–192 (2015).

63. Farin, H. F. *et al.* Visualization of a short-range Wnt gradient in the intestinal stem-cell niche. *Nature* **530**, 340–343 (2016).

64. Steele-Perkins, G. *et al.* The Transcription Factor Gene *Nfib* Is Essential for both Lung Maturation and Brain Development. *Molecular and Cellular Biology* **25**, 685–698 (2005).

65. Canals, I. *et al.* Rapid and efficient induction of functional astrocytes from human pluripotent stem cells. *Nat Methods* **15**, 693–696 (2018).

66. He, Y. *et al.* Spatiotemporal DNA methylome dynamics of the developing mouse fetus. *Nature* **583**, 752–759 (2020).

67. Hoadley, K. A. *et al.* Cell-of-Origin Patterns Dominate the Molecular Classification of 10,000 Tumors from 33 Types of Cancer. *Cell* **173**, 291-304.e6 (2018).

68. Patel, A. S. & Yanai, I. A developmental constraint model of cancer cell states and tumor heterogeneity. *Cell* **187**, 2907–2918 (2024).

69. Larsson, I. *et al.* Modeling glioblastoma heterogeneity as a dynamic network of cell states. *Molecular Systems Biology* **17**, e10105 (2021).

70. Varn, F. S. *et al.* Glioma progression is shaped by genetic evolution and microenvironment interactions. *Cell* **185**, 2184-2199.e16 (2022).

71. Capper, D. *et al.* DNA methylation-based classification of central nervous system tumours. *Nature* **555**, 469–474 (2018).

72. Berendsen, S. *et al.* Adverse prognosis of glioblastoma contacting the subventricular zone: Biological correlates. *PLoS ONE* **14**, e0222717 (2019).

73. Osswald, M. *et al.* Brain tumour cells interconnect to a functional and resistant network. *Nature* **528**, 93–98 (2015).

74. Ouspenskaia, T., Matos, I., Mertz, A. F., Fiore, V. F. & Fuchs, E. WNT-SHH Antagonism Specifies and Expands Stem Cells prior to Niche Formation. *Cell* **164**, 156–169 (2016).

75. Huang, X. *et al.* Transventricular delivery of Sonic hedgehog is essential to cerebellar ventricular zone development. *Proc. Natl. Acad. Sci. U.S.A.* **107**, 8422–8427 (2010).

76. Sirko, S. *et al.* Injury-specific factors in the cerebrospinal fluid regulate astrocyte plasticity in the human brain. *Nat Med* **29**, 3149–3161 (2023).

77. Jakab, M. *et al.* Lung endothelium exploits susceptible tumor cell states to instruct metastatic latency. *Nat Cancer* **5**, 716–730 (2024).

78. Sugihara, R., Kato, Y., Mori, T. & Kawahara, Y. Alignment of single-cell trajectory trees with CAPITAL. *Nat Commun* **13**, 5972 (2022).

79. Do, V. H. *et al.* Dynamic pseudo-time warping of complex single-cell trajectories. *bioRxiv* (2019) doi:10.1101/522672.

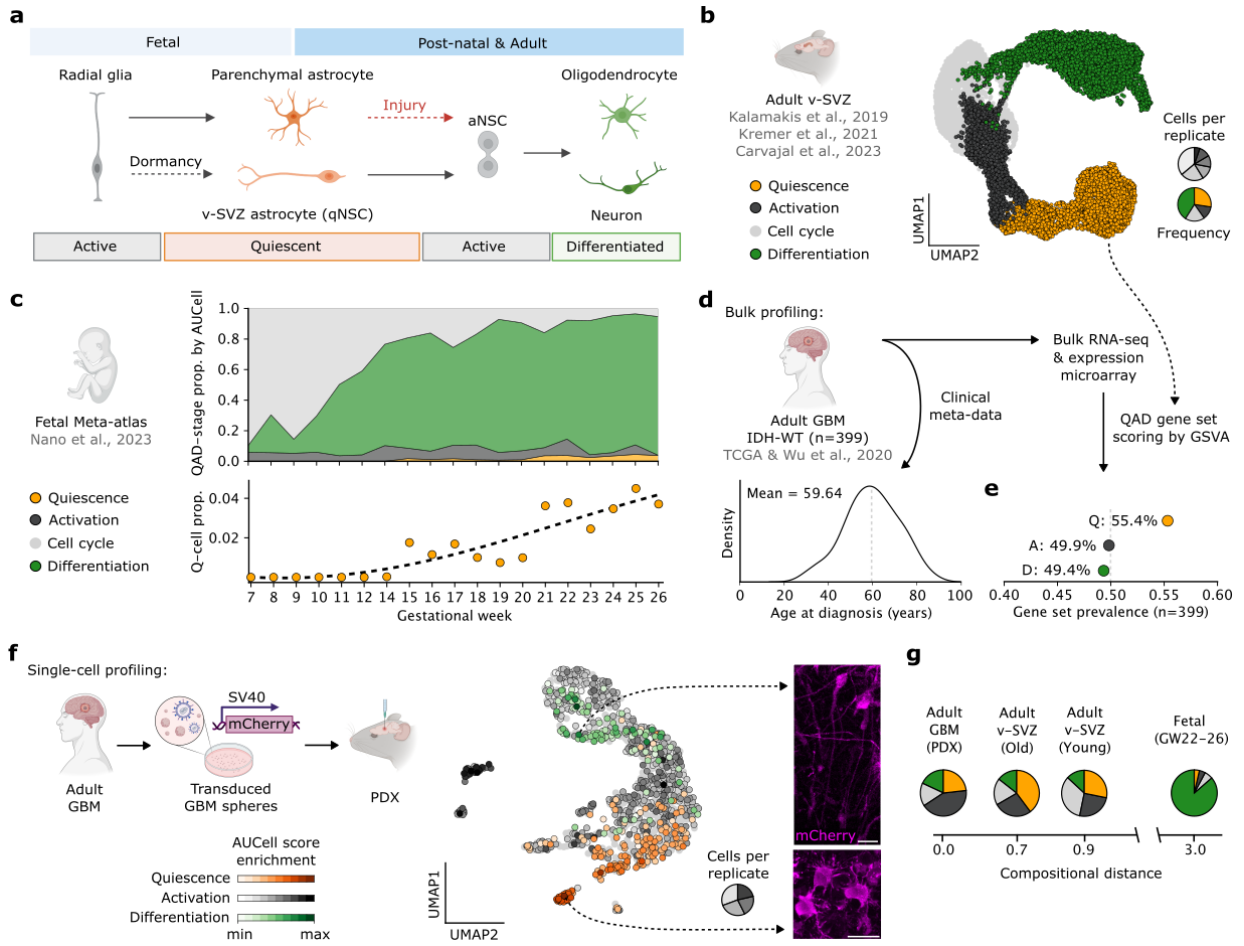

Fig. 1 | Activation state architecture (ASA) in the fetal and adult mammalian brain.

a Schematic representation of the embryonic origins of adult v-SVZ astrocytes (qNSCs) and parenchymal astrocytes along with their lineage potential in adulthood under homeostatic and injury conditions, respectively.

b UMAP embedding of integrated WT mouse v-SVZ NSC lineage scRNA-seq[15,19,40] (n=6 replicates), showing NSC differentiation trajectory through quiescence, activation, and differentiation (QAD) stages.

c Proportion of QAD-stage cells during human cortical development[41], with trend of Q-cell proportions shown below. Stage assignment by QAD-gene AUCell score.

d Distribution of age at diagnosis for n=399 primary GBMs in TCGA[43] and Wu et al[24].

e Non-parametric QAD-gene set scoring of multi-modal expression measurements of GBMs from (d). Gene set prevalence denotes the proportion of GBMs having a positive GSVA score.

f Left: Schematic of GBM patient derived xenograft (PDX) generation. mCherry ubiquitously labels tumor cells. Center: UMAP of single-cell GBM PDX (n=4 replicates) showing QAD-gene set AUCell scores. Cells are colored by the maximum-scoring state, enrichment relates the margin between the maximum and second-highest scores. Right: Representative immunofluorescence images of PDX GBM cells with distinct neuron- and astrocyte-like morphologies (dashed arrows). Scale bars 25μm.

g Aitchison compositional distance between QAD-stage frequencies in GBM PDX from (f) and young/old adult v-SVZ from (a) and late second trimester from (c).

v-SVZ: ventricular-subventricular zone; q/aNSC: quiescent/active neural stem cell.

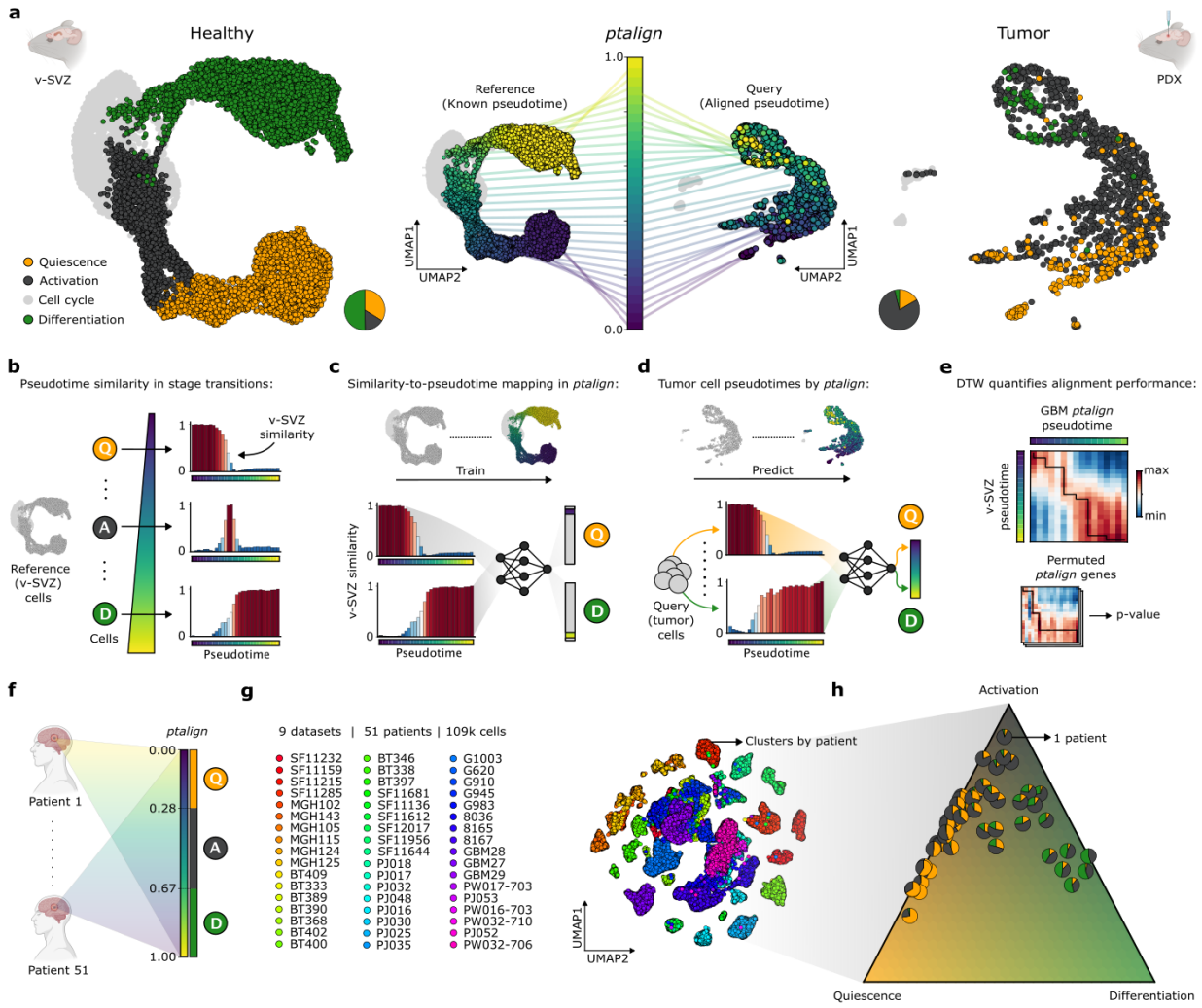

Fig. 2 | ptalign decodes the ASA of GBMs using the adult NSC lineage as a reference.

a Left: UMAP embedding of integrated WT mouse v-SVZ NSC lineage scRNA-seq (n=6 replicates), showing NSC differentiation trajectory through quiescence, activation, and differentiation (QAD) stages. Center: v-SVZ lineage pseudotime acts as a reference into which query GBM cells are mapped by ptalign. Colored lines depict pseudotime-binned cells linked to their average position in UMAP. Right: UMAP of GBM patient derived xenograft (PDX, n=4 replicates) with ptalign-derived QAD-stages. Cycling cells (gray) are excluded in pseudotime analysis. Pie charts indicate QAD-stage proportions.

b A pseudotime similarity metric derived from expression correlation along the v-SVZ lineage captures different stages and transitions by their characteristic similarity-profiles.

c In ptalign, a neural network is trained to predict v-SVZ lineage pseudotime based on similarity-profiles derived from the masked reference.

d Query tumor cell pseudotimes are assigned based on neural network predictions of v-SVZ similarity profiles. QAD-stage is derived based on the ptalign pseudotime value.

e ptalign performance is quantified by dynamic time warping (DTW), while a permutation framework tests for alignment robustness. DTW values represent the transcriptome correlation of reference and tumor cells binned in pseudotime.

f ptalign outlines a comparative view of tumor hierarchies, mapping patient samples within a single reference trajectory and enabling their comparison in that context.

g scRNA-seq UMAP of n=51 primary GBMs (Table S1, Fig. S4), colored by patient.

h Ternary plot of GBMs from (g) arranged by ptalign QAD-stage proportion, unveiling the underlying QAD-stage heterogeneity.

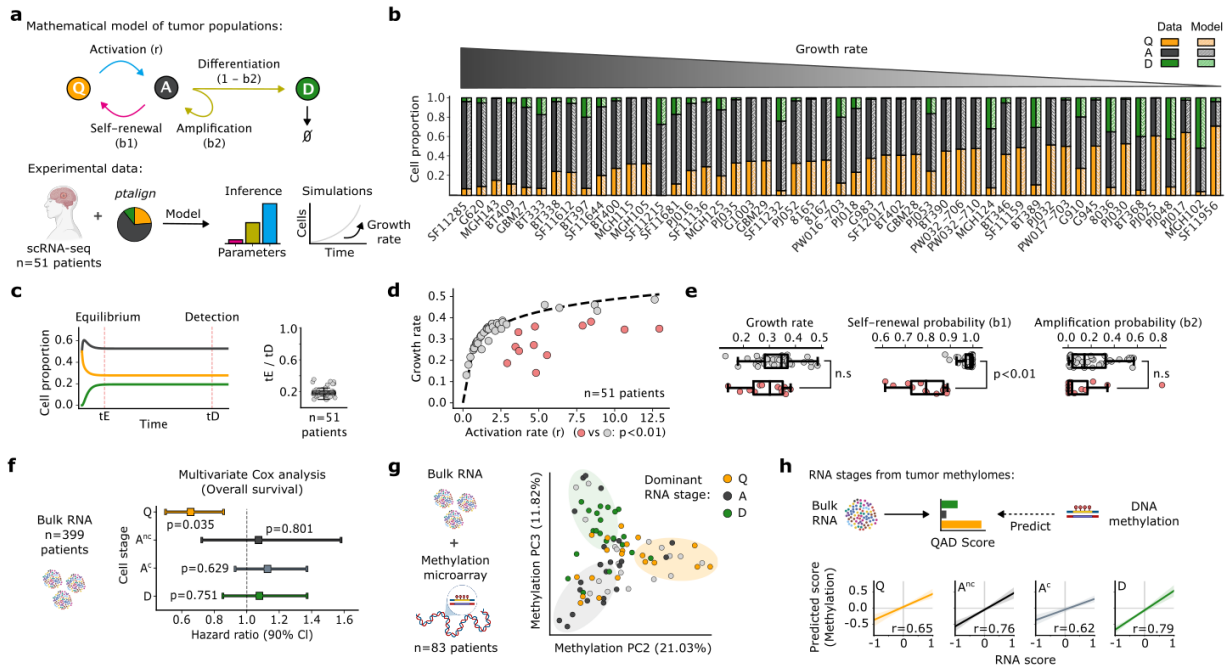

Fig. 3 | ASA informs GBM growth dynamics, prognosis and DNA methylation-based stratification.

a-b Application of v-SVZ population models[19,58] to GBM QAD-stage structure by ptalign, inferring descriptive parameters (a) and simulating growth to quantify growth rate among n=51 primary scRNA-seq GBMs (b).

c Left: Model simulated cell stages over time for example tumor in (a). QAD-populations reach steady-state equilibrium (tE) and grow until detection (tD, at 10^{11} cells). Right: tE/tD ratios across tumors in (b).

d-e Model simulated activation- and inferred growth rates for n=51 primary GBMs. Dotted line shows logarithmic fit of growth rate among GBMs (d). Tumors with high-residuals are shown in red, with the group-wise difference in growth rate and other model parameters shown in (e). Statistical significance was assessed by t-test.

f Predicted hazards and 90% confidence interval from a Cox model of n=399 bulk GBMs from TCGA[43] and Wu et al[24], with age and sex covariates of overall survival by GBM-QAD signature scores.

g PCA embedding of variable methylation sites for n=83 GBMs from (f) with matched RNA and methylome measurements. Tumors are colored by their dominant RNA-stage; gray circles have no clear dominant stage. Localized stage-enrichments are underscored with ellipses.

h ElasticNet prediction and 90% confidence interval of a (n=28) holdout set of RNA QAD-scores predicted from methylomes in (g). Models were trained on a (n=55) cohort. Pearson correlations (r) are indicated.

A^{nc}: active non-cycling; A^{c}: active cycling.

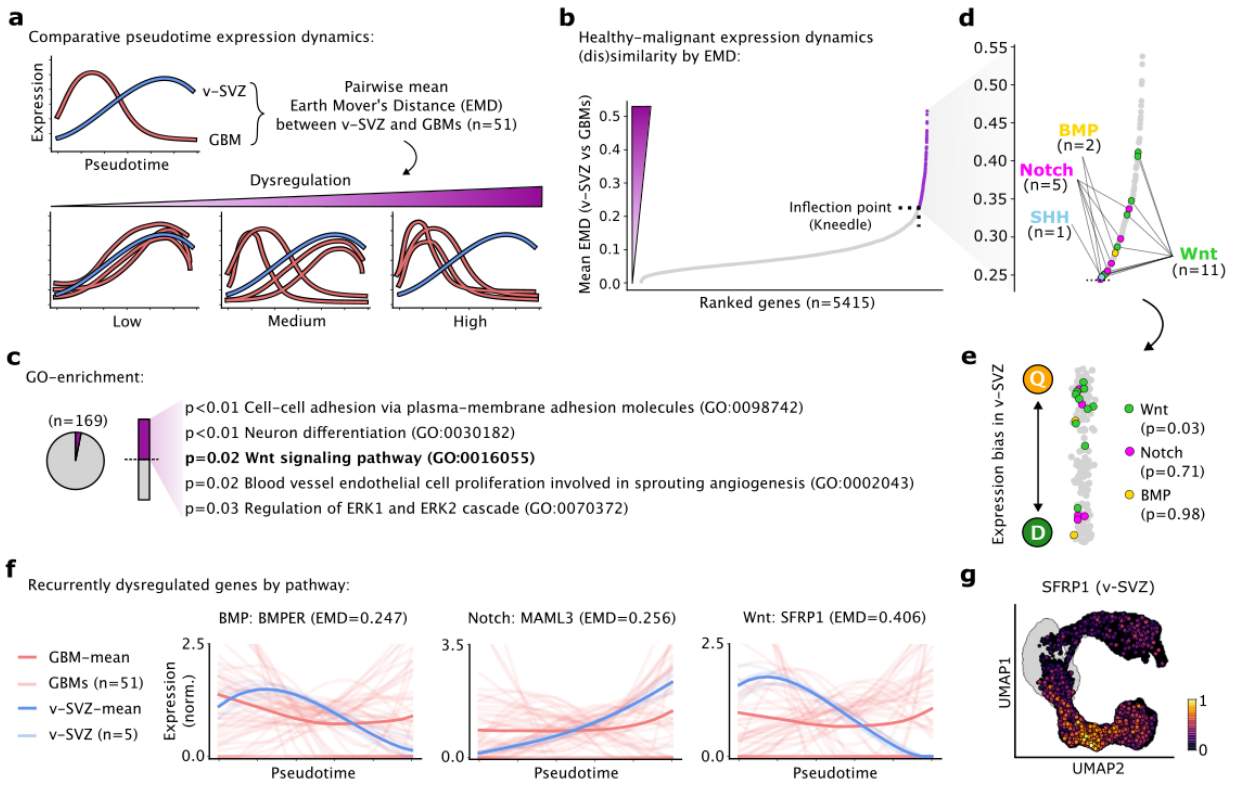

Fig. 4 | Comparative analysis of expression dynamics reveals recurrently dysregulated pathways in GBM.

a Shared ptalign axis between GBMs and v-SVZ enables comparative assessment of healthy vs malignant expression dynamics by pairwise Earth Mover's Distance (EMD). Mean EMD across GBMs informs gene dysregulation among GBM cohort.

b Genes ranked by mean EMD vs v-SVZ among n=51 GBMs. Genes above inflection point (n=164, purple) are considered recurrently dysregulated.

c GO enrichment of recurrently dysregulated genes from (b) with all considered genes as background. P-values are FDR-adjusted.

d Zoomed view of recurrently dysregulated genes from (b) with key signaling pathway genes indicated.

e v-SVZ expression bias for recurrently dysregulated genes from (b), colored by pathway-genes from (d). P-values represent Q-bias by permutation test.

f Expression splines and EMD values for individual genes from (d). Individual- and 95% confidence interval of mean GBM expression dynamics are colored red while v-SVZ dynamics are blue.

g Log-normalized SFRP1 expression in the v-SVZ UMAP is shown. Cycling cells are colored gray.

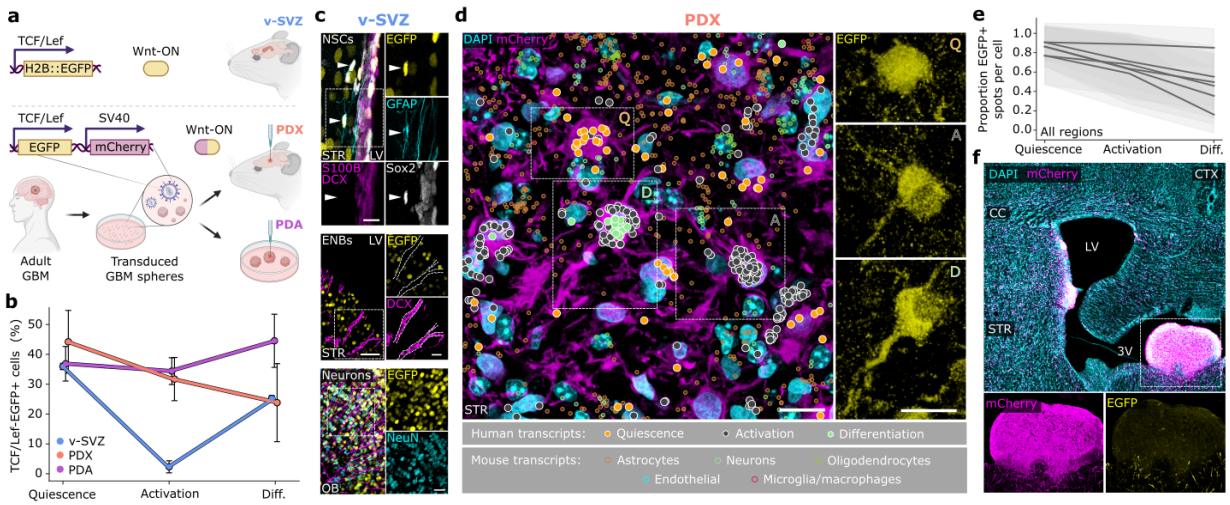

Fig. 5 | Dysregulation of Wnt activity at the Q-A transition in GBM.

a TCF/Lef-EGFP constructs reporting canonical Wnt signaling activity in v-SVZ NSCs from a transgenic mouse line (top) and by lentiviral vector (bottom) in PDX and PDA tumors. mCherry ubiquitously labels tumor cells.

b TCF/Lef-EGFP activity quantified in QAD-stage v-SVZ NSCs (n=1,564 cells, n=5 replicates) and T6 PDX (n=1,176 cells, n=4 replicates) and PDA (n=12,378 cells, n=4 replicates) cells. Reporter activity was quantified by FACS and QAD-stage by scRNA-seq. Errorbars represent standard deviation in the normalized Wnt-active cell proportion.

c Representative immunofluorescence images of TCF/Lef-H2B::EGFP activity for v-SVZ lineage populations. Top: NSCs lining LV identified by presence of GFAP, SOX2, EGFP and absence of S100B and DCX (scale bar 10μm). Middle: ENBs (scale bars 50 and 20μm) in v-SVZ marked by presence of DCX and absence EGFP. Bottom: EGFP+ LNBs and neurons in OB (scale bar 20μm).

d Representative spatial transcriptomics view of QAD-stage cells in a GBM PDX. Left: striatal section of clustered cells from QAD-stages overlaid with DAPI and mCherry immunofluorescence. Tumor transcripts are colored by QAD-stage with a white outline; mouse transcripts are colored by cell type. Right: QAD-stage cell EGFP fluorescence. Scale bars, 10μm.

e Mean fraction of EGFP+ spots for QAD-stage cells in n=6 spatial transcriptomics ROIs.

f Immunofluorescence image of GBM PDX tumor cells (mCherry) in a large ventricular outgrowth of the third ventricle. Scale bar, 250μm. Insets highlight tumor cells devoid of Wnt activity (left), which is regained upon entry to the brain parenchyma (right).

ENB: early neuroblast; LNB: late neuroblast; STR: striatum; LV: lateral ventricle; OB: olfactory bulb; CTX: cortex; CC: corpus callosum; 3V: third ventricle.

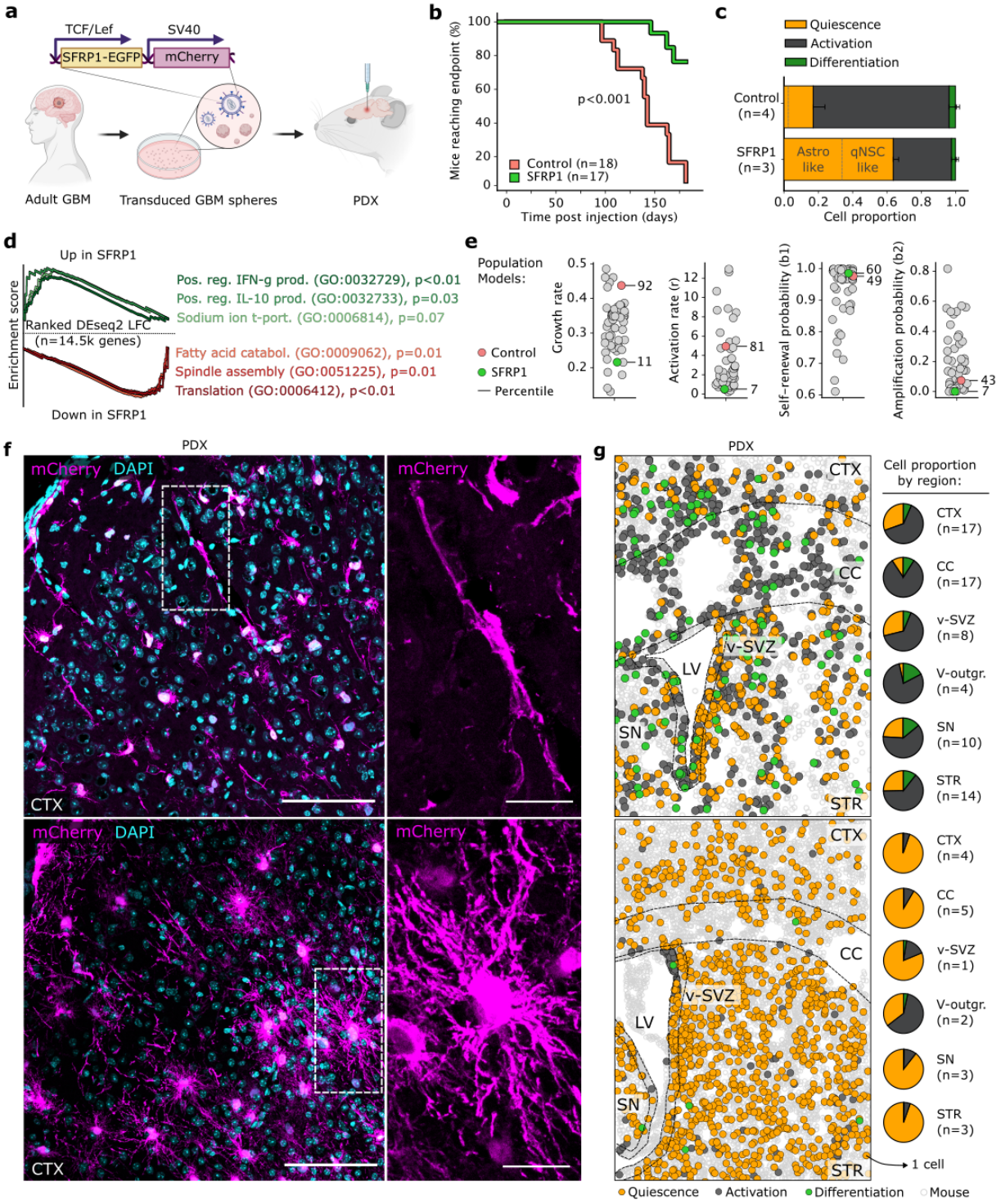

Fig. 6 | Targeted disruption of ASA by SFRP1 renders the tumor quiescent.

a SFRP1-overexpressing (OE) lentiviral construct used to generate GBM PDXs. mCherry ubiquitously labels tumor cells.

b Kaplan-Meier curve of mice reaching endpoint post injection among 3 batches of n=6 for control and SFRP1-OE mice each. P-value from log-rank test.

c Proportion of QAD-stage cells identified by ptalign in SFRP1-OE (n=3 replicates) and control (n=4 replicates) scRNA-seq. Error bars represent standard deviation.

d Selected GSEA enrichments from genes ranked by DEseq2 log fold-change between pseudobulked SFRP1-OE and control from (c). P-values are FDR-adjusted.

e Parameter estimates from population models of GBM dynamics (Fig. 3), including activation- and inferred growth rates as well as self-renewal and amplification probabilities for T6 control and SFRP1-OE GBM PDXs from (c) among n=51 primary GBMs. Rank percentile for each parameter is indicated.

f Representative immunofluorescence images of GBM cells in a control and SFRP1-OE (e) PDX brain. Scale bars 100μm, in insets 25μm.

g Entire spatial transcriptomics ROI depicting similar regions in SFRP1-OE (g) and control PDX brains. Transcripts were associated to segmented nuclei to assign species and QAD-stage. Pie charts indicate sum of QAD-stage cells by brain region across ROIs.

ROI: region of interest; CTX: cortex; CC: corpus callosum; LV: lateral ventricle; V-outgr.: ventricular outgrowth; SN: septal nuclei; STR: striatum.

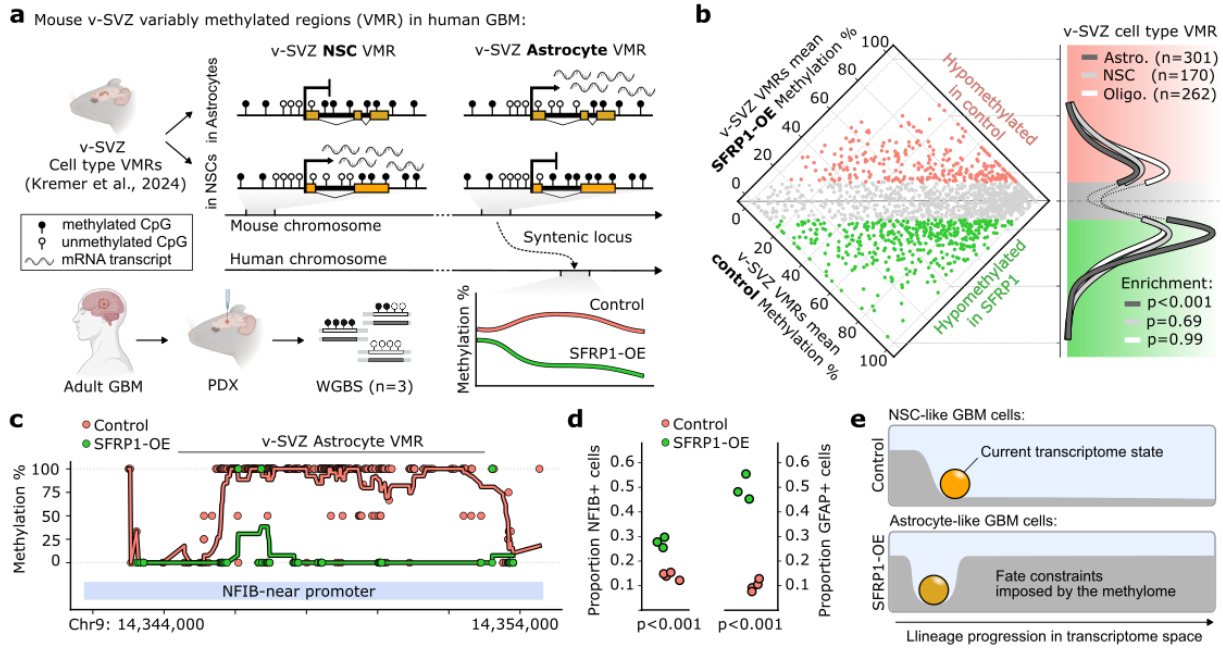

Fig. 7 | Emergence of a conserved astrocyte-like methylome in GBM cells by sFRP1.

a Cross-species interrogation of murine v-SVZ cell type VMRs from Kremer et al[32]. Example NSC and astrocyte VMR methylation profiles are depicted, with methylation at the corresponding human locus quantified in SFRP1-overexpressing (OE) and control GBM WGBS.

b Left: Mean methylation of v-SVZ cell type-specific VMRs from [32] in SFRP1-OE and control WGBS (n=3 technical replicates each). Differentially methylated regions are highlighted by genotype. Right: v-SVZ cell type VMRs in a Gaussian KDE over the vertical axis of the scatterplot. P-value by hypergeometric test.

c Selected v-SVZ astrocyte VMR overlapping an NFIB-promotor in SFRP1-OE and control. Points depict mean CpG methylation among replicates, lines comprise a 10-CpG moving average.

d Proportion of NFIB+ (left) and GFAP+ (right) Q-cells among control and SFRP1-OE samples. P-value by t-test.

e Schematic representation of the lineage potential in NSC-like GBM cells in control (above) vs lineage restrictions imposed by the remodeled methylome of the expanded astrocyte-like GBM cells upon SFRP1-OE (bottom).

VMR: variably methylated region.

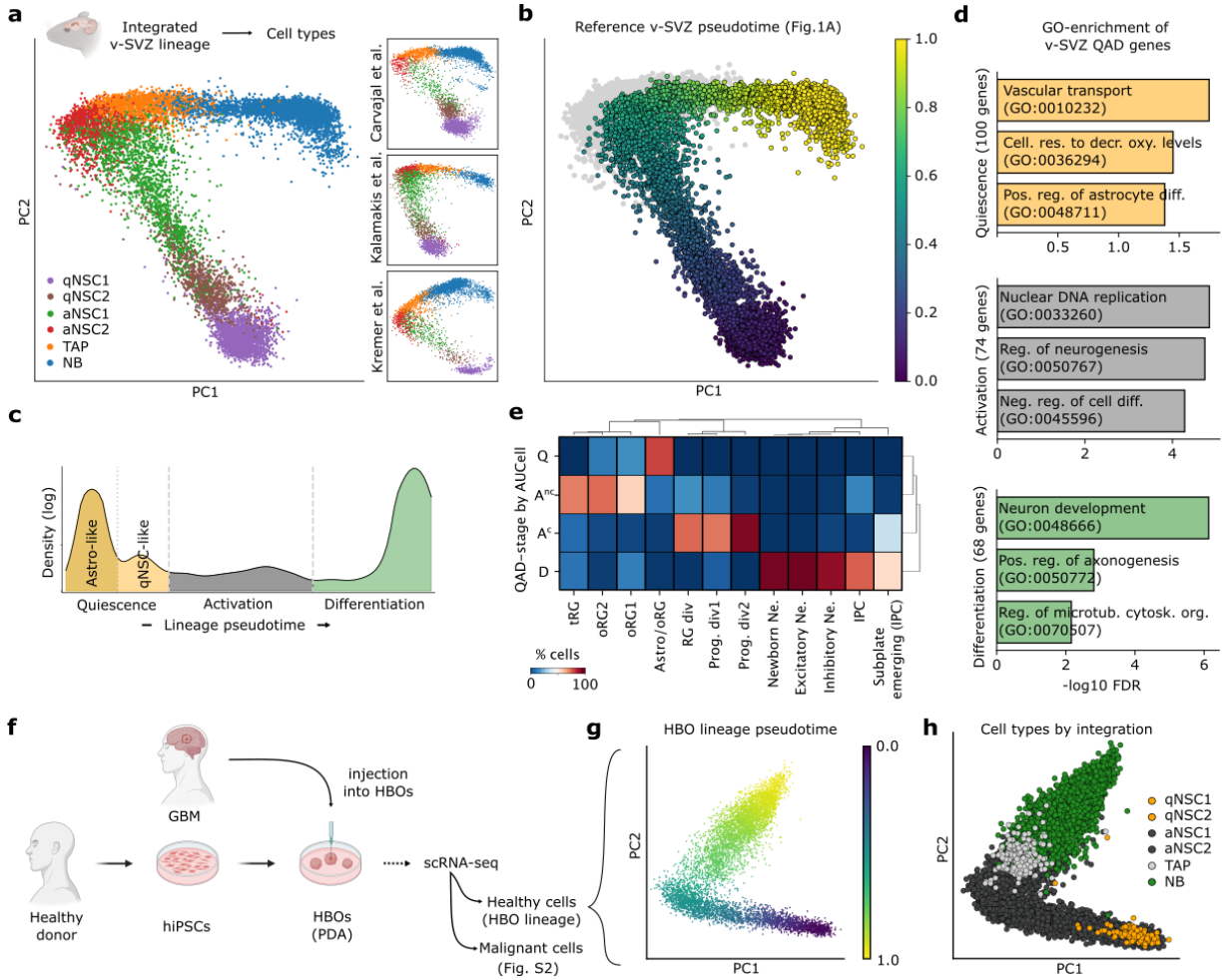

Fig. S1 | Adult murine v-SVZ NSC lineage QAD stages and their counterpart in human cortical development

a Left: PCA of integrated v-SVZ NSC lineage cells from Fig. 1a with cell types from [15] obtained by label transfer. Right: lineage datasets[15,19,40] with consistent transitions captured by PCA.

b Diffusion pseudotime fit on v-SVZ NSC lineage PCA in (a), used as the NSC reference pseudotime. Cycling cells are colored gray.

c Pseudotime cell density for NSC lineage from (b) by Gaussian KDE, with valleys denoting boundaries between QAD-stages. The Q-stage is subset into dormant astrocyte-like (Astro-like) and qNSC-like subsets based on the separation of qNSC1 and qNSC2 in (a).

d Selected GO-enrichments for SVZ-QAD genes by cell stage. P-values are FDR-adjusted.

e Overlap of QAD-stage and cycling cells with selected cell types from the human cortical development meta-atlas[41]. QAD-stage was determined by AUCell score-max.

f Scheme of the generation of PDA tumors by injection of GBM cells into HBOs. Healthy (see Fig. S3) and malignant (see Fig. S2) populations are identified by inferCNV (Methods).

g-h PCA of the integrated HBO NSC lineage dataset with diffusion pseudotime (g) and cell types by integration[11] (h). Note similarities to lineage stages in (a-b).

NB: neuroblast; TAP: transit amplifying progenitor; RG: radial glia; Ne.: neuron; IPC: intermediate progenitor cell; PDA: patient-derived allograft; HBO: human brain organoid; hiPSC: human induced pluripotent stem cell.

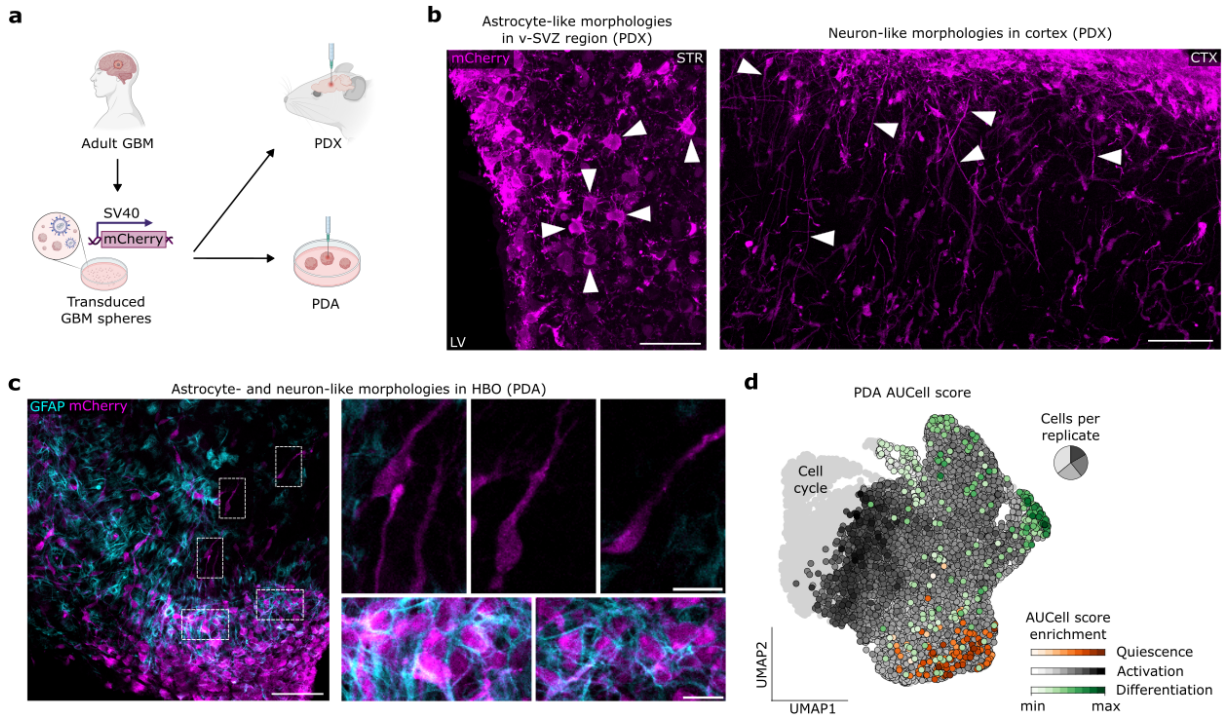

Fig. S2 | QAD stage inference in T6 PDX and PDA tumors

a Generation of T6 PDX tumors by orthotopic injection into mouse brains. TCF/Lef-EGFP reports canonical Wnt signaling while mCherry ubiquitously labels tumor cells.

b Representative immunofluorescence images of GBM cells in a T6 PDX, 5.5 mpi. Arrowheads highlight tumor cell morphologies in the v-SVZ (left) and cortex (right). Scale bars 100μm.

c Representative immunofluorescence images of GBM cells in a T6 PDA, 2 wpi, with tumor cell morphologies highlighted. mCherry labels GBM cells. Scale bars 100μm, in insets 25μm.

d AUCell scoring of T6 PDA cells (n=4 replicates) as in (c). Cycling cells are colored gray.

PDX: patient derived xenograft; PDA: patient-derived allograft; mpi: months post-injection; wpi: weeks post-injection; STR: striatum; LV: lateral ventricle; CTX: cortex; HBO: human brain organoid.

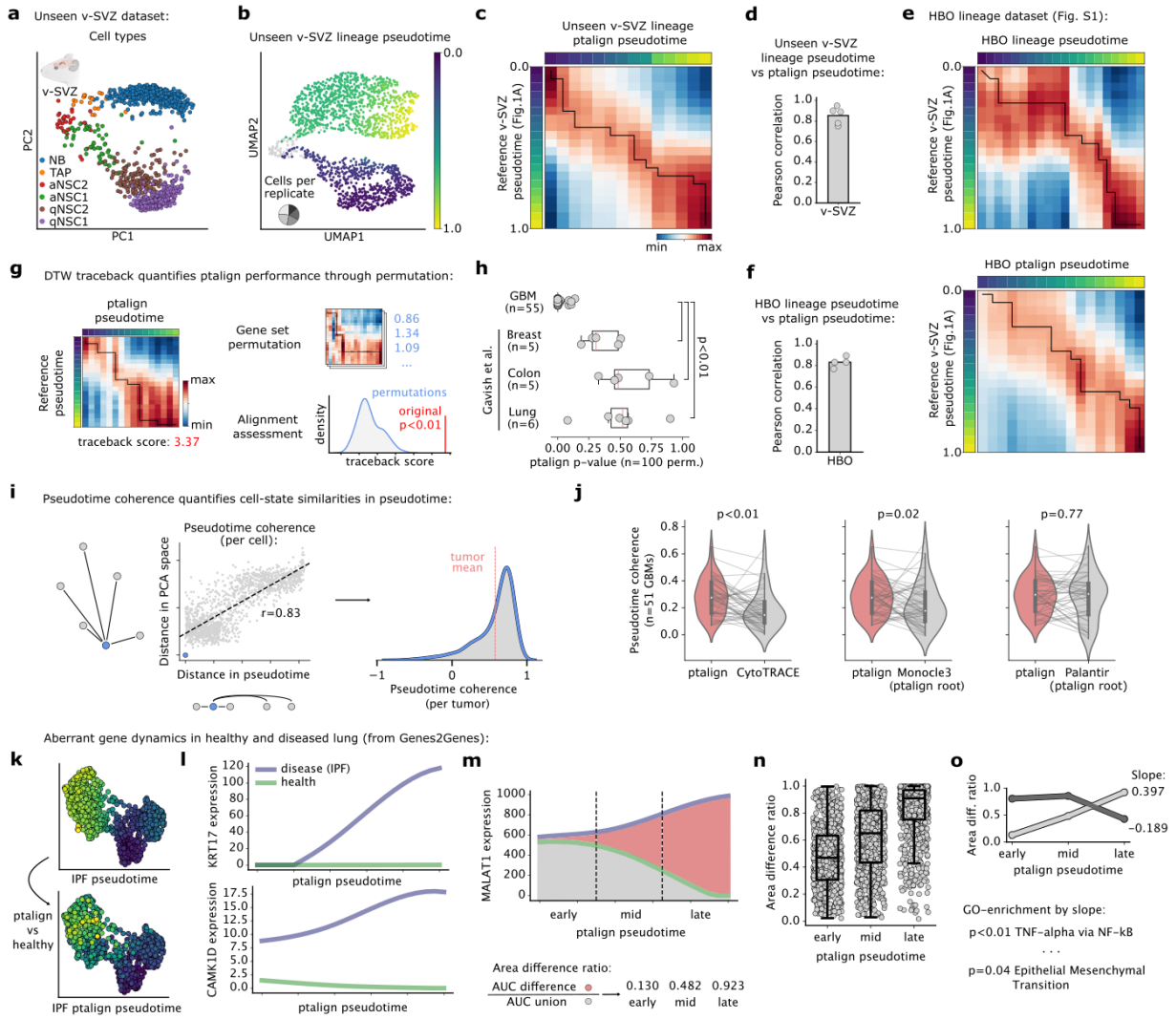

Fig. S3 | ptalign benchmarking by dataset and algorithm

a Expression PCA from n=5 replicates of an unseen v-SVZ NSC lineage dataset with cell types by label transfer[11].

b UMAP of the unseen v-SVZ NSC lineage from (a) with diffusion pseudotime. Cycling cells are colored gray.

c DTW denoting lineage similarity between the unseen v-SVZ NSC lineage pseudotime from (b) and the reference v-SVZ NSC lineage from Fig. 1a. DTW values represent pseudotime-binned cell's Pearson correlation.

d Pearson correlation in unseen v-SVZ lineage pseudotime (b) and ptalign pseudotime per replicate.

e Top: DTW of HBO NSC lineage diffusion pseudotime (Fig. S1) and the reference v-SVZ NSC lineage pseudotime (Fig. 1a). Bottom: DTW comparing the HBO ptalign pseudotime and v-SVZ NSC reference.

f Analogous to (d) for HBO lineage diffusion pseudotime and ptalign pseudotime.

g Permutation approach used to quantify ptalign performance. A DTW-score maximizing matrix traceback is compared for the original QAD and expression-matched permuted gene sets (Methods) to derive a permutation p-value.

h ptalign permutation p-values for 55 primary GBM scRNA-seq datasets (Fig. 1) and other tissue tumors[49].

i The pseudotime coherence metric compares distances in PCA space and pseudotime for each tumor. The correlation between each tumor cell (blue) and all other tumor cells (gray) is computed per cell, then averaged to derive a coherence score per tumor (right).

j Pseudotime coherence values for ptalign pseudotimes and named algorithms on 55 GBMs from (h). Scores for individual GBMs are linked. Statistical significance was assessed by paired t-test.

k Top: Pseudotime for IPF cells and, Bottom: ptalign pseudotime for IPF cells aligned to healthy lung reference from [47]

l Expression splines for selected genes with variable dynamics in healthy and IPF lung, as reported in Genes2Genes[47] on the ptalign pseudotime.

m-n Area difference ratio in pseudotime increments exemplified by MALAT1 (m) and shown across genes (n).

o Slope of area difference ratio over pseudotime increments represents fluctuating expression divergence. GSEA by slope reveals enriched EMT genes among positive slopes. P-values are FDR-adjusted.

HBO: human brain organoid; DTW: dynamic time warping; IPF: idiopathic pulmonary fibrosis.

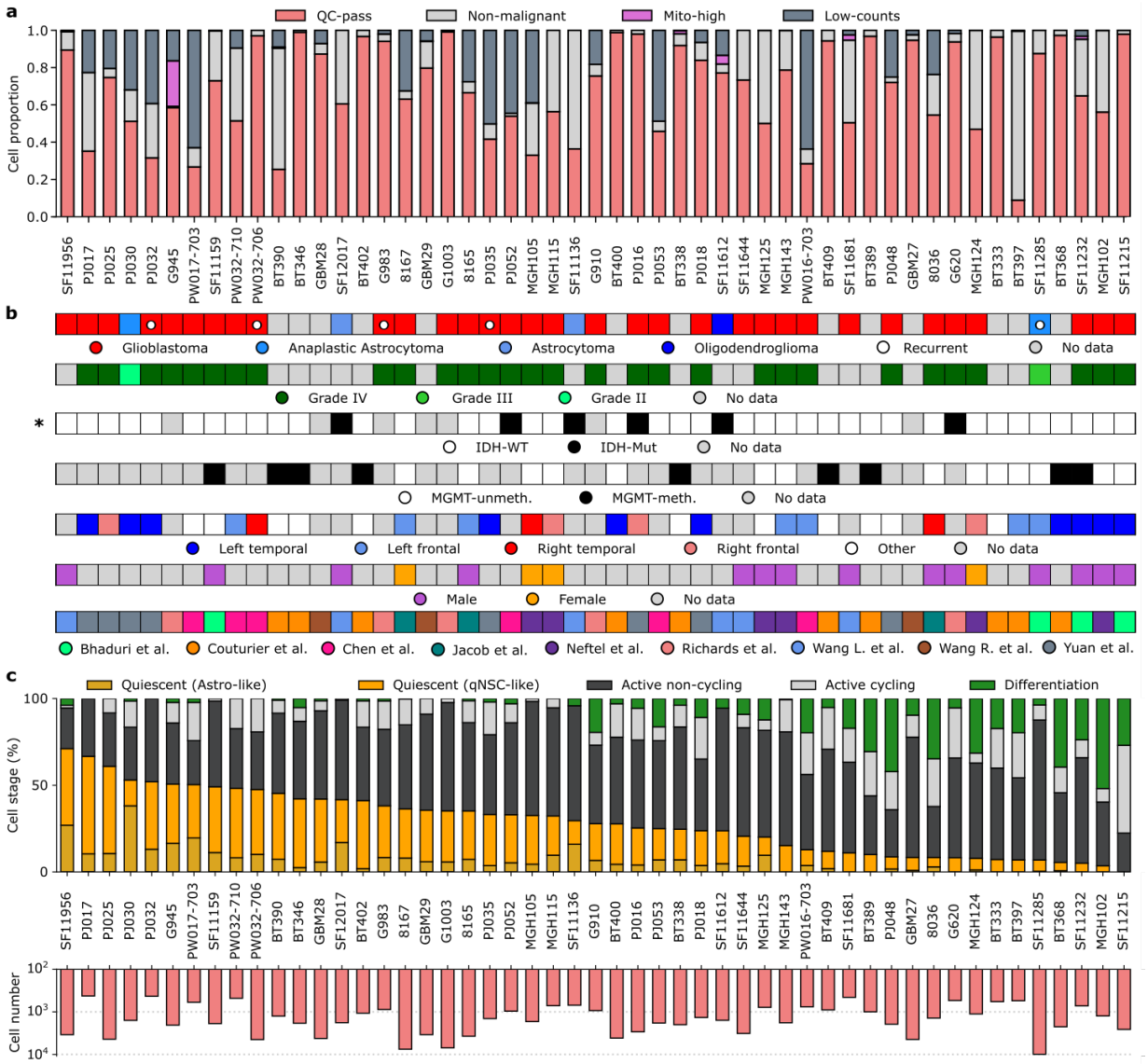

Fig. S4 | External GBM scRNA-seq datasets metadata and ASA

a Barcharts relating proportion of cells filtered in QC-steps for published primary GBM scRNA-seq datasets (n=51, Table S1) that pass ptalign permutation threshold.

b Collated patient metadata across studies for tumor diagnosis, stage, IDH-mutation status, MGMT-methylation status, location, and sex. Asterisk (*) indicates significant association with QAD-stage by ANOVA.

c Top: stacked barcharts depicting the proportion of cells assigned to QAD stages from ptalign pseudotimes, with Q-stage cells subset by Astro-like and qNSC-like stages. Cycling cells are colored gray. Bottom: number of cells assigned a ptalign pseudotime for each tumor. Each column in A-C relates information from the same tumor.

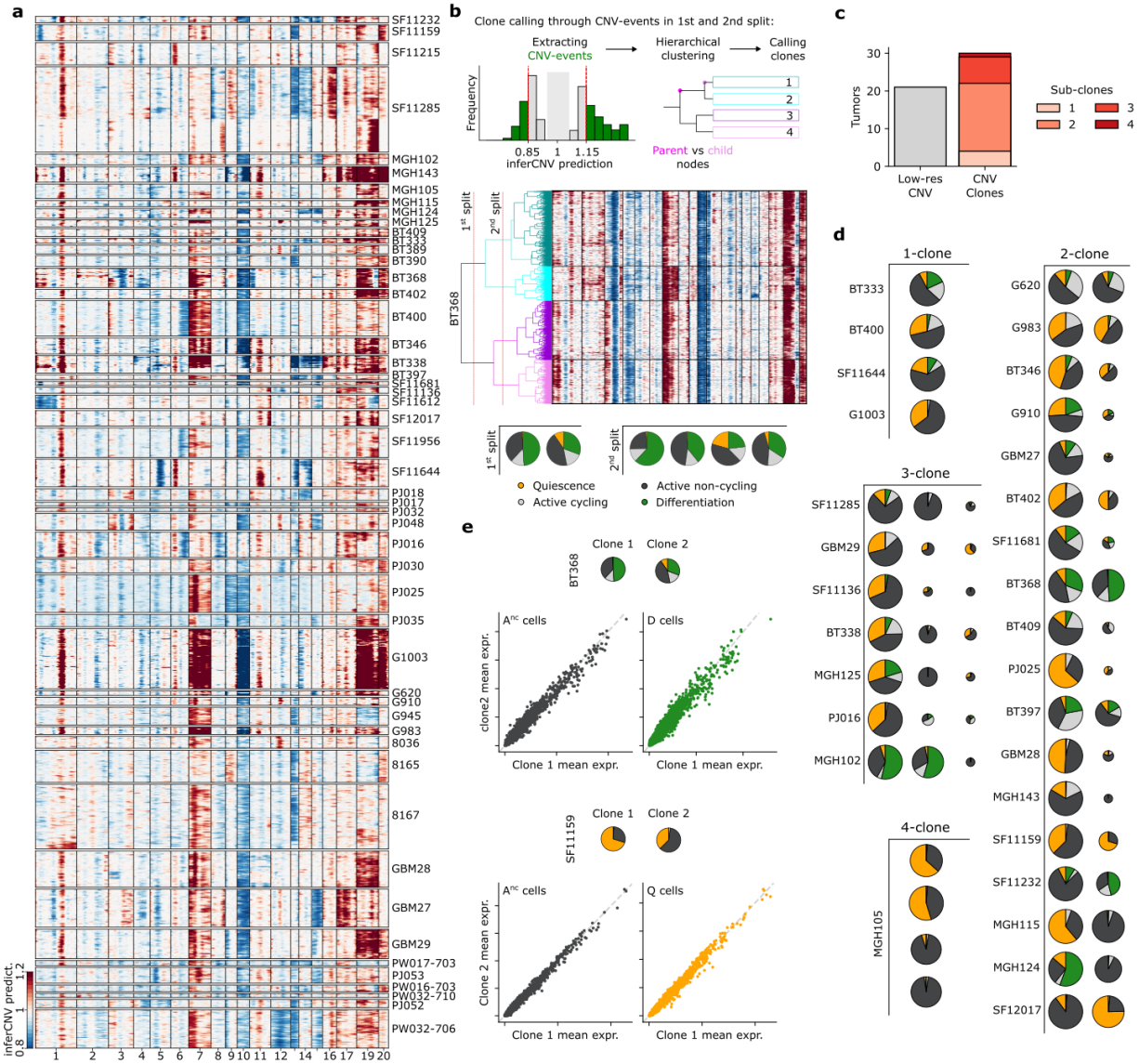

Fig. S5 | CNV clones exhibit consistent QAD-stage transcriptomics

a Copy number variation (CNV) landscape by inferCNV of n=51 primary GBM tumors. CNV losses (blue) and gains (red) are arranged by chromosome (columns) and separated by tumor into cells (rows). Cells per tumor were hierarchically clustered by CNV-profile, with each 5th cell shown (of n=109,079 total). Sex chromosomes are not shown.

b Schematic representation of clone assignment for tumor BT368. CNV-events are determined by thresholding inferCNV predictions and used to compare parent vs. child nodes in the 1st and 2nd split of a CNV-based hierarchical clustering to derive 1-4 clones per tumor (see Methods).

c Barchart depicting CNV-clones assigned for individual GBMs. Clone assignment in Low-res tumors was inconclusive.

d Proportion of QAD-stage and cycling cells per clone per tumor. Pie chart size relates relative clone size.

e Gene expression in QAD-stage cells from two clones in BT368 (top) and SF11159 (bottom) denoted by pie charts. Scatterplots depict mean log-normalized expression of pseudobulk QAD-stage cells per clone, for all expressed genes.

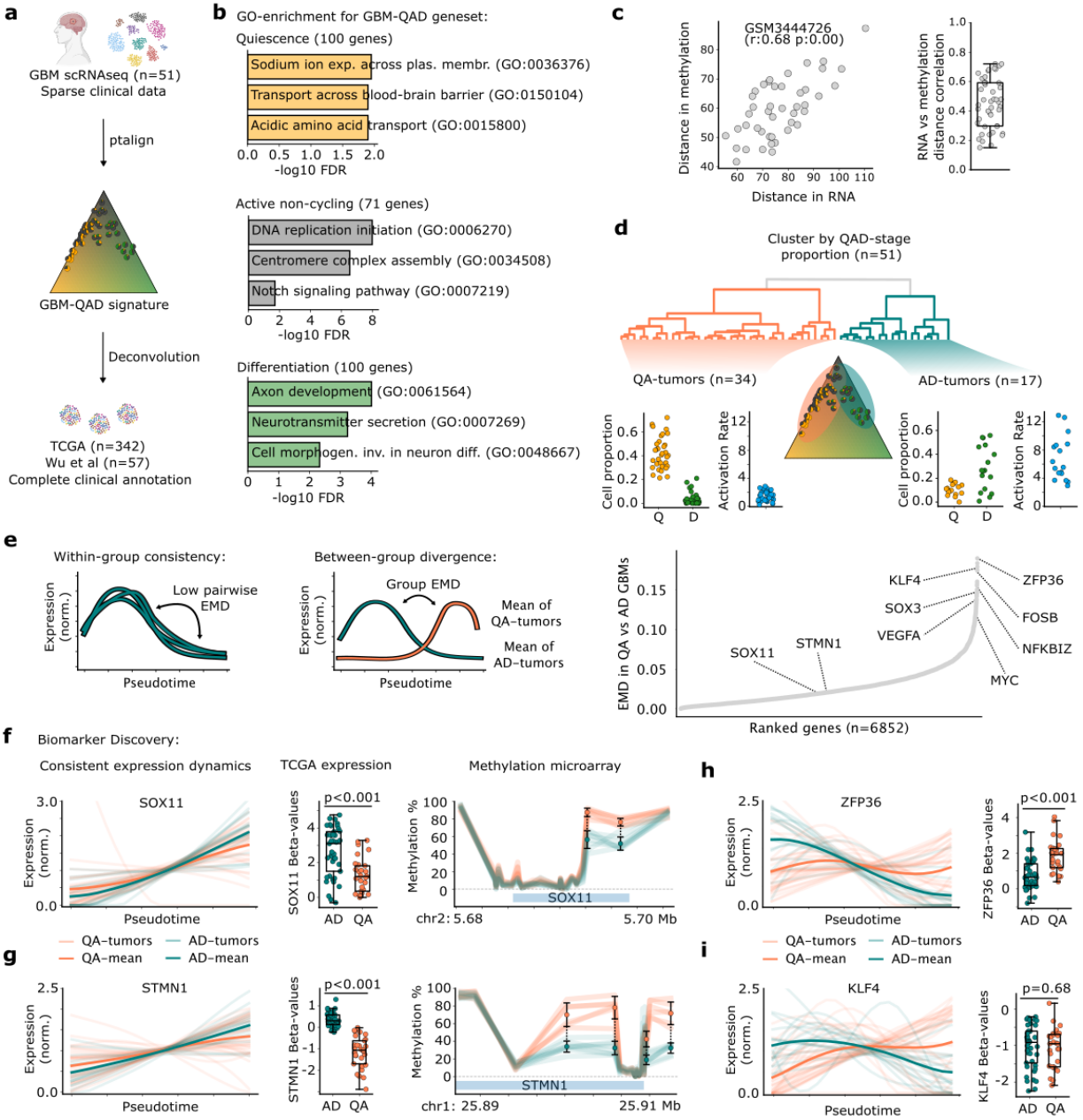

Fig. S6 | Leveraging expression heterogeneity in GBMs to identify genes with consistent and divergent expression dynamics

a As scRNA-seq GBM datasets lack clinical metadata these are supplemented from bulk TCGA and Wu et al datasets through deconvolution.

b Selected terms from GO-enrichment of GBM-QAD genes derived from n=51 scRNA-seq GBMs (see Methods).

c Inter-tumoral euclidean distances in methylation- and RNA-modalities for a selected tumor from vs. other Wu et al[24] tumors (left) with Pearson correlation and p-value indicated; and across tumors (right).

d Supporting patient stratification by clustering GBMs by QAD-stage, separating tumors into Q-biased (QA-) and D-biased (AD-) groups with varying activation rates in v-SVZ population models.

e Left: Strategy for detecting group-specific expression dynamics: comparing between-group divergence while maximizing within-group consistency using the Earth Mover's Distance (EMD) for QA- and AD-groups from (g). Right: per-gene EMD average between QA- and AD-tumor groups. Relevant genes are indicated.

f-g Supporting SOX11 (f) and STMN1 (g) as biomarkers for QA- vs AD-tumors. Each exhibits consistent pseudotime expression dynamics (left), group-specific expression in TCGA (center), and variable methylation (right). Methylation n=6 replicates in QA and n=8 in AD, from ellipses in Fig. 3g.

h-i Expression splines for divergent QA- and AD-tumor genes ZFP36 (h, left) and KLF4 (i, left) and their group specific expression in TCGA (right). Dark line represents group-mean with 95% confidence interval.

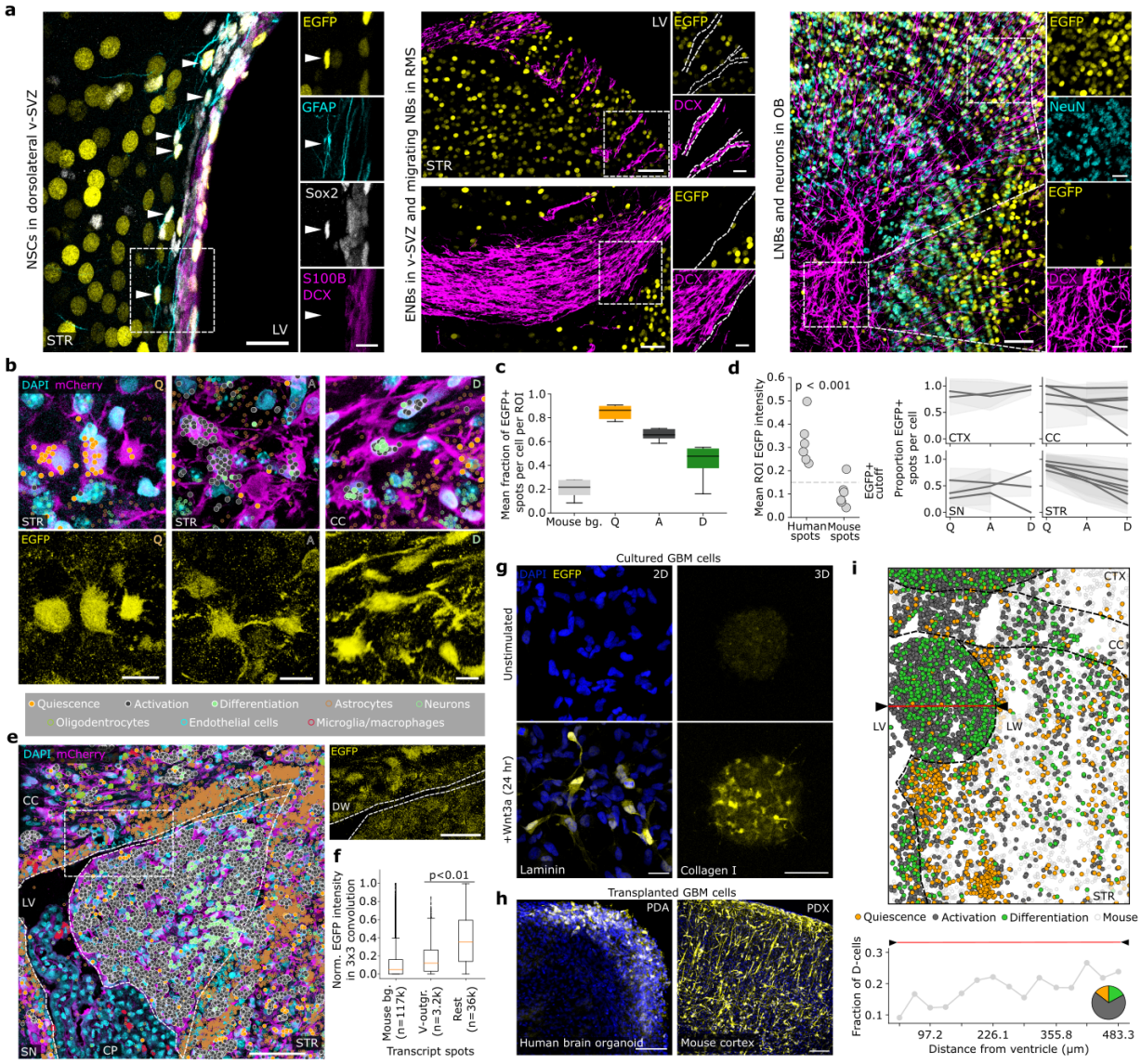

Fig. S7 | Canonical Wnt signaling in healthy and malignant NSC lineages

a Full immunofluorescence images for Fig. 5, depicting TCF/Lef-H2B::EGFP activity for v-SVZ NSCs (left; coronal view; scale bars, 20 and 10µm), ENBs (NBs; center; sagittal view; scale bars, 50 and 20µm), and LNBs and neurons (right; sagittal view; scale bars, 50 and 20µm). Arrows identify v-SVZ NSCs by presence of GFAP, SOX2 and absence of S100B and DCX.

b Selected Q (left), A (center), and D (right) cells in spatial transcriptomics with transcripts overlaid with DAPI and mCherry (top) or EGFP (bottom) immunofluorescence. Scale bars, 10µm.

c Mean fraction of EGFP+ spots among pixels in mouse and QAD-stage cells for n=6 spatial transcriptomics ROIs.

d EGFP+ spot threshold (left) and proportion of EGFP+ spots by QAD-stage in individual brain regions with >20 cells (right) from n=6 spatial transcriptomics ROIs. Significance was assessed by t-test, shaded area represents 90% confidence interval.

e Left: Wnt-reporter spatial transcriptomics ROI of a ventricular outgrowth. Transcriptomic markers are overlaid with DAPI and mCherry immunofluorescence. Scale bar, 50µm. Right: EGFP fluorescence the ventricle edge. Scale bars, 25µm.

f Normalized EGFP-intensity for mouse background (bg.) and tumor cells within (V-outgr.) and outside (rest) a ventricular growth seen in (e, n=1). Significance was assessed by permutation test.

g Wnt-reporter GBM cells (EGFP+) on laminin coated chambers (left; scale bar, 25µm) or as 3D spheroids in collagen matrix (right; live, unstained; scale bar, 100µm), 24h post recombinant-Wnt3a treatment.

h Wnt-reporter GBM cells (EGFP+) transplanted into HBOs (left, 10dpi) or mouse brains (right, 5mpi). Scale bars, 100µm.

i Top: large ventricular growth in a non-Wnt-reporter spatial transcriptomics ROI with transcripts associated to segmented nuclei to assign species and QAD-stage. Red line traces largest extent from LW to LV. Bottom: increasing D-cell fraction in cells binned by distance to ventricle. Pie chart depicts QAD-stage proportions within the growth.

ENB: early neuroblast; LNB: late neuroblast; STR: striatum; RMS: rostral migratory stream; OB: olfactory bulb; AC: astrocyte; CC: corpus callosum; CTX: cortex; SN: septal nuclei; LV: lateral ventricle; CP: choroid plexus; DW: dorsal-wall; d/mpi: days/months post injection.

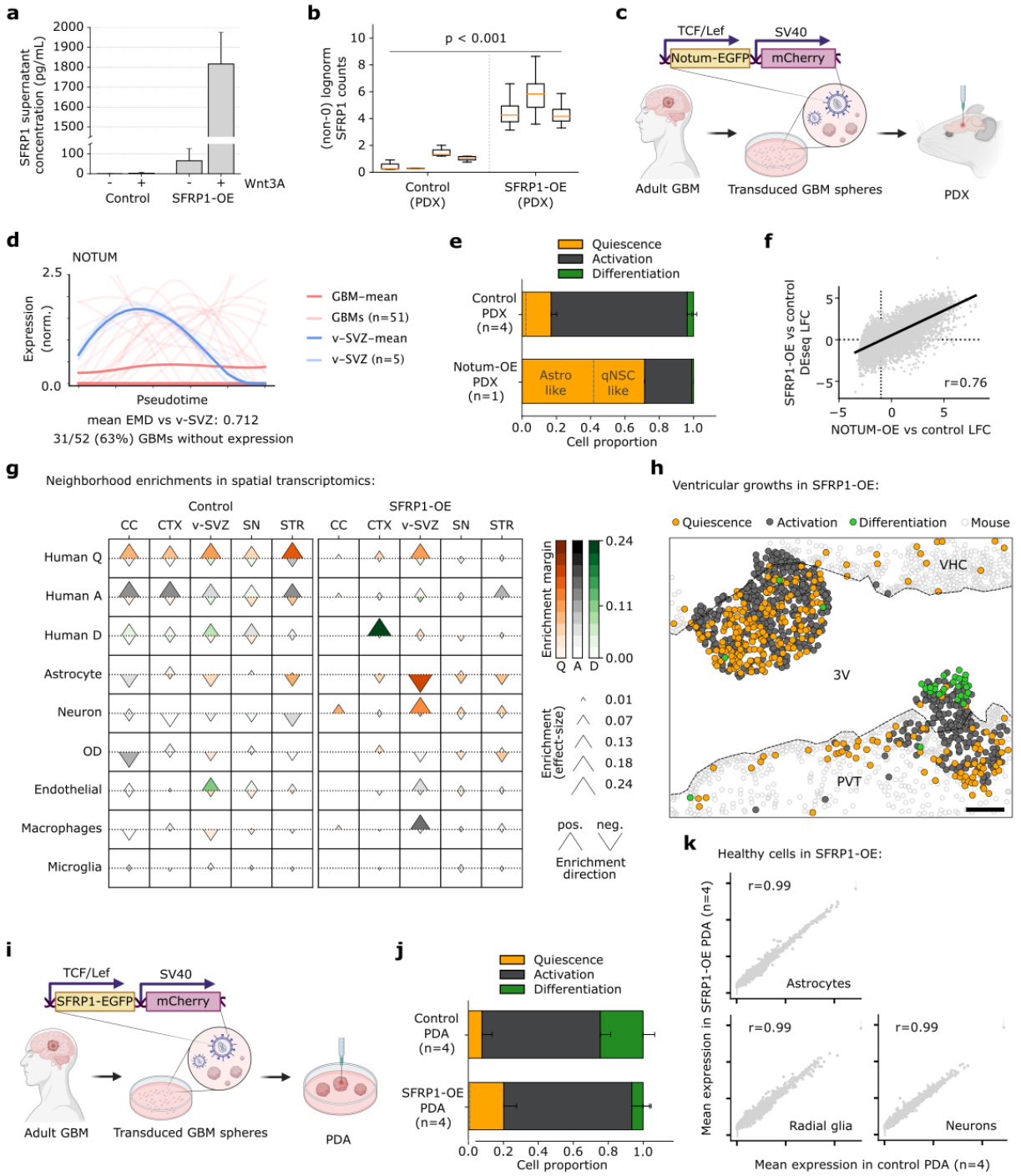

Fig. S8 | Characterization of SFRP1-based intervention in preclinical models of GBM

a SFRP1 concentration by ELISA in supernatant of cells stimulated with/without Wnt3A. Error bars represent standard deviation in n=3 replicates.

b Normalized SFRP1 expression levels in SFRP1-OE cells, by genotype. Significance was assessed by t-test.

c NOTUM-OE construct used in T6 PDA tumor. mCherry ubiquitously labels tumor cells.

d NOTUM dysregulation in n=51 tumors by expression splines as in Fig. 4. Excluded from previous analysis as most GBMs lose NOTUM expression.

e Proportion of QAD-stage cells by ptalign in control (n=4 replicates) and NOTUM-OE (n=1) PDA cells. Error bars represent standard deviation.

f NOTUM-OE log fold-change against SFRP1-OE DEseq2 log fold-change (LFC). Black line indicates best fit, Pearson correlation (r) is indicated.

g Neighborhood enrichment by permutation (Methods) for segmented cells in n=17 Wnt-reporter and n=6 SFRP1-OE spatial transcriptomics ROIs. Cell type enrichments are reported for QAD-stage cells with other cell types (rows), with enrichment direction by shape and strength by size, while color relates the enrichment margin between the largest and second-largest enrichments.

h Zoomed SFRP1-OE spatial transcriptomics ROI with QAD-stage cells in two ventricular outgrowths. Transcripts were associated to segmented nuclei to assign species and QAD-stage. Scale bar, 10μm.

i-j SFRP1-OE construct used in T6 PDA tumors as in (c), with ptalign QAD-stage cells 14-dpi in SFRP1-OE (n=4 replicates) and control (n=4 replicates) PDA cells (j). Error bars represent standard deviation.

k Mean log-normalized expression in control and SFRP1-OE PDA healthy astrocytes (left), radial glia (center) and neurons (right). Pearson correlation is indicated.

OE: overexpressing; AC: astrocyte; RG: radial glia; CTX: cortex; CC: corpus callosum; SN: septal nuclei; STR: striatum; 3V: third ventricle; VHC: ventral hippocampal commissure; PVT: periventricular nuclei of the thalamus: dpi: days post injection.

Methods

Experimental Models

Culture of Human 293T Cells

293T cell line was used for production and titration of the lentiviral particles. 293T cell line is a fast growing, highly transfectable derivative of human embryonic kidney 293 cells. Due to the presence of SV40 large T antigen, they allow high levels of proteins to be expressed therefore are ideal for generating high-titer lentiviral particles.

293T cells were maintained in Dulbecco's Modified Eagle's Medium (DMEM) supplemented with 10% FCS, 1% penicillin/streptomycin (10,000 units/mL) and 1% L-Glutamine (200 mM) at 37C and 5% CO_2.

Culture and Maintenance of Human iPSCs

The human iPSCs were acquired from Allen Institute for Cell Science (AICS-0036-006, https://www.allencell.org/cell-catalog.html). The AICS-0036-006 line was labeled with EGFP via CRISPR/Cas9 system, where mEGFP transgene was knocked in chromosome 19q13-qter. Their parental cell line (https://www.coriell.org, GM25256) was acquired from Coriell (UCSFi001-A, https://labs.gladstone.org/conklin/) and was derived from a healthy donor using an episomal reprogramming method[1].

iPSCs were feeder-independent and Matrigel (Corning, 354277) was employed to coat the plates or dishes. iPSCs were maintained on mTeSR1 medium (Stem Cell Technologies, 05850 or 100-0276) at 37˚C and 5% CO_2. ReLeSR™ (Stemcell Technologies, 05872) was used for passaging cells, with media change every other day.

Patient Tumors and Tumor Sphere Culture

Primary tumor samples were received from the University Hospital Ulm upon obtaining informed consent prior to surgery. Experiments involving patient tumor biopsies were carried out in accordance with the Declaration of Helsinki and were approved by the ethics committees of Heidelberg University, Medical Faculty Mannheim (S-224/2021). All tumor specimens were examined by a neuropathologist to ensure that the tumors met GBM criteria defined by the World Health Organization. Upon arrival, fresh tissues were immediately dissociated using Brain Tumor Dissociation Kit (P) and expanded in culture. Tumor spheres were maintained in serum-free Neurobasal A medium supplemented with B27, heparin (2 µg/ml) and the stem mitogens EGF (20 ng/ml) and bFGF (20 ng/ml) at 5% CO_2 and 37°C. For passaging, tumor spheres were enzymatically dissociated into single cells using Accutase when sphere size reached approximately 100 µm in diameter approximately once in a week.

Mouse Strains

Male TCF/Lef:H2B/GFP mice[2] were bred at the Center for Preclinical Research at the German Cancer Research Center and were used for analyzing TCF/Lef-activity in mouse NSC studies. Male Fox Chase SCID Beige mice (CB17.Cg-Prkdc^{scid}Lyst^{bg-J}/Crl) were purchased from Charles

River and were used to generate human-mouse xenograft tumors. Experimental mice had *ad libitum* access to food and water and were housed in specific pathogen-free, light (12 hr day/night cycle), temperature (21°C) and humidity (50–60% relative humidity) controlled conditions. In addition, daily monitoring of mice for symptoms of disease determined the time of sacrificing for injected animals with signs of distress. All procedures were approved and conform to the regulatory guidelines of the official committee (Regierungspräsidium Karlsruhe, Germany; G19/21).

Lentiviral Transduction

Human GBM cells were transduced with the 7TGC (Addgene plasmid #24304), 7TGC-SFRP1 or 7TGC-Notum lentiviral vectors at a multiplicity of infection (MOI) of 5. Expression of the transduction marker (mCherry) was confirmed by FACS analysis. Second-generation, replication deficient lentiviral particles were produced, purified and titrated as described previously[3].

Immunocytochemistry

For 2D culture of human GBM cells, $3x10^5$ cells in 0.3 mL of Neurobasal A medium were seeded into each well of µ-Slide 8-well chamber (Ibidi). Prior to seeding, the wells were coated with 10 µg /ml poly-D-Lysine overnight at the room temperature, washed 3 times with DPBS and subsequently coated with 10-20 µg/ml Laminin for 2 hours at 37 °C. The cells were treated with a recombinant Wnt3a (200 ng/mL dissolved in 0.1% bovine serum albumin (BSA) in distilled water). 0.1% BSA was used in carrier-only conditions as baseline controls. Following 24 hr post-treatment, the cells were washed 3 times with DBPS and fixed with 2% PFA for 20 minutes at the room temperature. Next, the fixed cells were incubated in permeabilization/blocking solution (0.25% Triton-X 100 in PBS supplemented with 3% horse serum and 0.3% BSA) for one hour at room temperature to block unspecific binding sites. Subsequently cells were stained with anti-GFP antibody in blocking buffer overnight at 4°C. After washing 3 times 5 min with 0.25% Triton-X 100 in PBS, secondary antibody staining was carried out using appropriate Alexa-fluorophore antibodies diluted in blocking buffer for 1 hour at the room temperature. DAPI was added to the antibody cocktail for nuclear staining. Furthermore, cells were washed 3 times 15 min with 0.25% Triton-X 100 in PBS. After mounting with Fluoromount-G, slide was allowed to dry in dark at room temperature for 30 min. Samples were stored in the dark at 4°C until imaging.

For 3D culture of human GBM cells, individual tumor spheres of approximately 100 µm in diameter were seeded in 0.1 mL of Collagen matrix containing 0.27 mg of Collagen type I (Corning; rat tail) supplemented with 10% minimum essential medium (MEM; 10x) and 20% NaOH (0.1 M) for pH adjustment in a well of 10-well cell view cell culture slide (Greiner Bio-one). Collagen matrix was allowed to polymerize for 1 hr at 37°C and 0.3 mL of Neurobasal A medium with recombinant Wnt3a (200 ng/mL in 0.1% BSA in distilled water) or carrier-only (0.1% BSA in distilled water) was added for 24 hr before live-imaging.

Confocal images were acquired on a Leica TCS SP5 or SP8 confocal microscope at the light microscopy facility of the German Cancer Research Center. ImageJ was used for processing and images were only adjusted for brightness and contrast.

Molecular Cloning of 7TGC-SFRP1 and 7TGC-Notum Constructs

Human SFRP1 (Origene plasmid #RC207328) or Notum (Gateway ORF clone ID #164485821) was clonned in frame under 7xTCF promoter (7TGC; Addgene plasmid #24304) upstream of EGFP sequence using In-Fusion HD cloning kit according to manufacturer's instructions. A furine cleavage site (RKRR) as well as a self-cleaving peptite linker (P2A) was incorporated between SFRP1/Notum and EGFP to allow seamless protein translation avoiding fusions (S8.C and F). 7TGC plasmid was a gift from Roel Nusse. P2A-RKRR plasmid was a gift from Edward Green. Notum plasmid was obtained through the vector and clone repository[4] of the genomics and proteomics facility of the German Cancer Research Center. Constructs cloned as part of this study are available from the investigators upon request.

Enzyme-linked Immunosorbent Assay (ELISA) for SFRP1

T6 Wnt-reporter or SFRP1-OE GBM cells ($5x10^5$ per well) were seeded in a 6-well plate in Neurobasal A medium. The cells were treated with a recombinant Wnt3a (dissolved in 0.1% bovine serum albumin (BSA) in distilled water at a final concentration of 200 ng/mL). 0.1% BSA was used in carrier-only conditions as baseline controls. Following 24 hour post-treatment, the supernatant was collected and the ELISA protocol was followed according to manufacturer's instructions (Abcam; ab277082). The optical density (OD) of the samples was measured at 450 nm with the plate reader (Agilent Biotek). The respective concentration of each sample was calculated based on the standard curve generated by known protein concentrations and measured optical density (OD) at 450 nm following background subtraction according to manufacturer's instructions (Abcam; ab277082).

Human Brain Organoid Generation

The procedure was adapted from a previously published method[5,6,7]. Briefly, on day 0, hiPSCs were first dissociated into single cells and seeded in ultra-low attachment round-bottom 96-well plates (Corning, 7007), containing human embryonic stem cell (hESC) medium supplemented with 4 ng/ml bFGF (PeproTech, AF-100-18B-50) and 50 µM Rho-associated protein kinase (ROCK) inhibitor (Merck Millipore, SCM-075). On day 3, the medium was replaced with fresh hESC medium. From day 5, the embryoid bodies were transferred to ultra-low attachment 24-well plates (Corning, 3473) in Neural Induction Medium. On Day 11, organoids were embedded into droplets of Matrigel (Corning, 354234) and transferred into 6 well plates in another two-day Neural Induction Medium. Differentiation Medium without vitamin A was fed from day 13 to day 19. From day 20 on, organoids were cultured in Differentiation Medium with vitamin A. Agitation was employed from day 18 at 70 RPM and the medium was changed every 2-3 days.

Transplantation of GBM Cells for PDA Generation

For injection of retrovirally transduced primary GBM cells into human brain organoids, $5x10^4$ cells were cultured as single cell suspension overnight. Newly formed spheres were resuspended in 1 µl of Differentiation Medium with vitamin A, loaded into a NanoFil syringe and injected into the core of 2-3 month-old organoids under a dissection microscope. Tumor bearing organoids were

maintained in Differentiation Medium with vitamin A on an orbital shaker (70 RPM) for 15 days at 5% CO_2 and 37°C.

Orthotopic Injection of GBM Cells for PDX Generation

For orthotopic injection of retrovirally transduced (or untransduced control) primary GBM cells into the mouse brain, $5x10^5$ cells were cultured as single cell suspension overnight. Newly formed spheres were resuspended in 2 µl of Matrigel, loaded into a NanoFil syringe and stereotactically injected into the striatum (2.0 mm lateral to the bregma at a depth of 3.0 mm) of 8-10 week-old Fox Chase SCID-Beige mice under general anesthesia and perioperative pain management. Tumor growth was longitudinally monitored by magnetic resonance imaging (MRI) at the Small Animal Imaging Center of the German Cancer Research Center. Upon reaching termination criteria outlined in the approved animal experiment application, mice were sacrificed and brains were collected after transcardial perfusion.

For perfusion, mice were anesthetized by intraperitoneal injection of perfusion solution. After opening the thoracic cavity exposing heart, transcardial perfusion was carried out with ice cold HBSS.

Flow Cytometry Analysis and Fluorescence-activated Cell Sorting (FACS)

For isolation of TCF/Lef-EGFP reporter healthy v-SVZ-lineage; v-SVZ, rostral migratory stream (RMS) and olfactory bulb (OB) were dissected and single cell suspensions (n=5 mice) were prepared using Neural Tissue Dissociation Kit (P) and gentleMACS Octo Dissociator with Heaters (Miltenyi) according to manufacturer's instructions. To allow discrimination of different populations, single cell suspensions were stained with the following antibodies conjugated with appropriate fluorophores as previously reported[8]: anti-CD45, anti-Ter119, anti-O4, anti-Glast, anti-CD133 (Prom1) and anti-PSANcam including proper unstained, single stained and fluorescent minus one (FMO) controls. After excluding dead cells, doublets and CD45+/Ter119+/O4+ non-lineage populations; NSCs in the v-SVZ were gated based on Glast+vity and CD133+vity; early neuroblasts (ENBs) in the v-SVZ as well as late neuroblasts (LNBs) in the OBs were gated based on Glast-vity, CD133-vity and PSANcam+vity. Each population was index-sorted into 384 well-plates (Eppendorf Lobind) as single cells. Microplates containing cell lysates were briefly centrifuged, snap frozen on dry ice and were stored at -80°C until processed for Smart-seq3.

For isolation of the xenografted human GBM cells, tumor bearing mouse brains (5-7 mpi; n=8 mice in total; n=4 control; n=3 SFRP1-OE; n=1 Notum-OE) were dissected and single cell suspension was prepared using Brain Tumor Dissociation Kit (P) and gentleMACS Octo Dissociator with Heaters (Miltenyi) according to manufacturer´s instructions. Transduction marker mCherry was used to discriminate transduced human GBM cells while a human specific-MHCI antibody was employed to discriminate untransduced human GBM cells. After excluding dead cells and doublets, MHCI+ or mCherry+ (EGFP+ and EGFP-) cell population was index-sorted into 384 well-plates (Eppendorf Lobind) as single cells. Microplates containing cell lysates were briefly centrifuged, snap frozen on dry ice and were stored at -80°C until processed for Smart-seq3.

For isolation of human brain organoid and allografted human GBM cells, tumor bearing organoids were dissociated using Brain Tumor Dissociation Kit (P) and gentleMACS Octo Dissociator with Heaters (Miltenyi) according to manufacturer's instructions. Prior to multiplexing (n=8 HBOs), single cell suspensions were labelled with TotalSeqA anti-human hashtag oligonucleotide (HTO) antibodies (Biolegend, 1:50) to allow downstream de-multiplexing in silico as previously described[9]. After excluding dead cells and doublets, mCherry+ as well as mCherry- cell populations were sorted as bulk populations into 1.5 ml tubes (Eppendorf) and immediately processed for single cell RNA-sequencing using 10X Chromium 3' sequencing platform.

Sytox Blue (Life Technologies, 1:1000) was used in all experiments as a dead cell indicator. Index sorting of single cells as well as sorting of bulk samples was carried out using a 100 micron nozzle at a BD FACSAria II or BD FACSAria Fusion at the Flow Cytometry Core Facility at the German Cancer Research Center.

Single Cell Library Preparation with Smart-seq2/3

Single cell RNA-sequencing (scRNA-seq) libraries from v-SVZ-lineage populations were prepared using Smart-seq3 protocol as previously described (Hagemann-Jensen, Nature Biotechnology, 2020) with minor modifications. The protocol was automated and miniaturized by incorporating liquid handling platforms including Mosquito HV (SPTLabtech), Mantix (Formulatrix) and Viaflo 384 (Integra). Briefly, plates were incubated at 72°C for 10 min to facilitate lysis and denaturation of secondary structures in the RNA. Lysed cells were subjected to reverse transcription in 2 µl using Maxima H-minus reverse transcriptase (Thermo Scientific), an oligo(dT) primer and a template-switching oligonucleotide encompassing an 8-bp unique molecular identifier (IDT). In a randomly selected set of wells, we included ERCC Spike-ins (Ambion) at a 1:2,500,000 dilution. Full length cDNAs were amplified for 22 cycles of PCR using KAPA HiFi DNA polymerase (KAPA Biosystems). cDNA samples were purified with Ampure XP beads at a 1:0.8 ratio and cDNA quality in randomly selected 10 wells/plate was assessed on a High Sensitivity Bioanalyzer chip (Agilent). cDNA concentrations were quantified using Quant-it PicoGreen dsDNA Assay kit (Thermo Scientific) and Synergy LX multi-mode microplate reader (Biotek). cDNAs were normalized to 250-500 pg µl-1. 100-200 pg of cDNA per sample was used for tagmentation in 1.2 µl using Illumina XT DNA sample preparation kit. Libraries were finally amplified for 11 cycles of PCR in 4 µl using custom-designed Nextera index primers containing 8-bp index barcode sequences with a minimal Levenshtein distance of 4 as previously published[10]. Samples were purified with Ampure XP beads at a 1:0.8 ratio and DNA quality in randomly selected 10 wells/plate was assessed on a High Sensitivity Bioanalyzer chip (Agilent). Libraries were quantified as mentioned above and normalized libraries were equimolarly pooled and purified one last time at a 1:0.8 ratio. Prior to sequencing, final library concentration was determined using Qubit dsDNA High Sensitivity Assay kit (Thermo Scientific) and Qubit fluorometer (Invitrogen) and the average fragment size was calculated on a High Sensitivity Bioanalyzer chip (Agilent).

scRNA-seq libraries from PDXs were prepared initially prepared using Smart-seq2[11] (n=4) and later using Smart-seq3 protocol (n=6) as outlined above. Libraries with 1 % spiked-in PhiX control (Illumina) were sequenced at the 75-bp paired end on a high output flow cell using an Illumina

NextSeq550 instrument at a sequencing depth of ~1 M reads per cell at the sequencing open lab of the German Cancer Research Center.

Single Cell Library Preparation by 10x Chromium 3´ Sequencing

Single cell RNA-sequencing libraries from human brain organoids as well as patient-derived allografts were prepared using Chromium Next GEM Automated Single Cell 3´ Library and Gel Bead Kit v3.1 (10x Genomics) according to manufacturer's instructions at the single cell open lab at the DKFZ. In parallel, HTO libraries were prepared as previously described[9]. mRNA libraries with 2 % spiked-in PhiX control (Illumina) were sequenced at the 100-bp paired end on a P3 flow cell using an Illumina NextSeq2000 instrument at a sequencing depth of ~80 K reads per cell. HTO libraries with 40% spiked-in PhiX control were sequenced at the 75-bp paired end on a mid-output flow cell using an Illumina NextSeq550 instrument at a sequencing depth of ~2 K reads per cell at the sequencing open lab of the German Cancer Research Center.

Bulk Whole-genome Bisulfite Sequencing (WGBS)

Tumor bearing mouse brains (5-7 mpi) were additionally perfused with 4% PFA and post-fixed in 4% PFA overnight at 4°C. 50 µm coronal sections were prepared using a Vibratome VT1200S (Leica). Samples were stored in 0.01% NaN3 in PBS at 4°C until processing. The genomic DNA (gDNA) from 3 whole-brain sections per group was isolated by QiaAmp DNA microkit (Qiagen 1048145) and the concentrations were measured by Qubit DNA HS kit. The protocol for bisulfite conversion and library preparation was adapted based on the genomic part of the scNMT-seq protocol[12] with the following modifications. The gDNA input was adjusted to be 20 ng per sample. The number of first-strand purification cycles was decreased to 4 runs, and library amplification reaction was performed in 10 cycles. The library concentrations were measured by Qubit DNA HS kit and the fragment distribution was analyzed by the Bioanalyzer DNA HS kit (Agilent). Before sequencing, libraries were pooled equimolarly. The final pool with 15% spiked-in PhiX control was sequenced at the 150 bp paired end on a P2 flowcell using and Illumina NextSeq 2000 at a sequencing depth of 40M read per sample at the sequencing open lab of the German Cancer Research Center.

Immunofluorescent Staining and Microscopy

To visualize healthy v-SVZ-lineage, mouse brains were additionally perfused with 4% PFA post-fixed in 4% PFA overnight at 4°C. 50 µm coronal or sagittal sections were prepared using a Vibratome VT1200S (Leica). Samples were stored in 0.01% NaN_3 in PBS at 4°C until staining. For staining, sections were incubated in blocking solution for one hour at room temperature to block unspecific binding sites. Subsequently sections were stained with anti-GFP, anti-GFAP, anti-Sox2, anti-S100β, anti-DCX and anti-NeuN antibodies in blocking buffer overnight at 4°C on a rotator. After washing the sections 3 times 15 min with 0.25% Triton-X 100 in PBS, secondary antibody staining was carried out using appropriate Alexa-fluorophore antibodies diluted in blocking buffer for 1 hour at the room temperature. DAPI was added to the antibody cocktail for nuclear staining. Furthermore, sections were washed 3 times 15 min with 0.25% Triton-X 100 in PBS. After mounting with Fluoromount-G, sections were allowed to dry in dark at room temperature for 30 min. Samples were stored in the dark at 4°C until imaging.

To visualize PDX tumors, mouse brains were prepared, processed and imaged as outlined above. To visualize PDA tumors, HBOs were washed and fixed with 4% PFA for 1 hr at the room temperature, 10 dpi. Both PDA and PDX were stained with the following primary antibodies: anti-RFP, anti-GFP and anti-human-specific Nestin prior to imaging.

Confocal images and tile scans were acquired in a Leica TCS SP5 or SP8 confocal microscope at the Light Microscopy Facility of the German Cancer Research Center. ImageJ was used for processing and images were only adjusted for brightness and contrast.

Spatially Resolved Transcriptomics by Molecular Cartography (Resolve Biosciences)

For molecular cartography (MC) experiments, tumor bearing mice were additionally perfused with 4% PFA and post-fixed with 4% PFA overnight at 4°C. Samples were incubated in 15% and subsequently 30% sucrose solution overnight each at 4°C, respectively. OCT-embedded specimens were cryo-sectioned into 10 µm thick coronal sections onto MC slides. Permeabilization, hybridization and automated fluorescent microscopy imaging were performed according to the manufacturer's instructions for fix-frozen samples with minor modifications. Briefly, the slides were thawed at the room temperature and dried at 37°C in a thermal cycler with MC slide holder. Sticky wells were attached to the MC slide to create the MC observation chamber. The sections underwent various treatments excluding post-fixation but including permeabilization, rehydration, and application of TrueBlack autofluorescence quencher, which was diluted according to the instructions provided by Biotium. Following thorough washing and priming, specific probes designed by Resolve Biosciences' proprietary algorithm for our transcripts of interest (Sequences not listed here) were hybridized overnight at 37°C. The hybridized sections were washed again, and the MC observation chamber was placed in the MC machine for eight automated cycles of coloring and imaging to determine the transcript localization of our panel of 98 transcripts in the tissue. Regions of interest (ROIs) were selected for each section (Control vs sFRP1) based on a brightfield overview scan. To aid the ROI selection process, we additionally scanned consecutive sections of the MC sections following immunofluorescent staining with tumor specific markers. In the final imaging round, the nuclei were stained with DAPI to create a reference image for nuclei segmentation. After the run, the MC software registered the raw images, assigned transcripts to detected combinatorial color codes, and combined individual tiles to create ROI panoramas. The outputs consisted of text files containing the 3D coordinates of the transcripts and maximum projections of DAPI images for each ROI.

In order to complement the MC data with a panel of relevant proteins, processed sections were used to perform immuno-fluorescent labelling (as outlined above) of mCherry, EGFP and were counter-stained for DAPI. The same ROIs were tile-scanned using Leica SP5 and SP8 confocal microscope at the Light Microscopy Facility of the German Cancer Research Center and images from respective RNA-protein modalities were registered using the common DAPI staining in each panorama.

Data Analysis

Derivation of Integrated Adult WT SVZ NSC Lineage and Pseudotime

Our reference lineage includes adult WT SVZ NSCs and progeny from three studies[8,13,14], supplemented with data from another study[15] for comparison. All datasets were reduced to 16,598 human-mouse 1:1 orthologs using Ensembl 102[16], with human gene names representing mouse counterparts. Counts, excluding the supplemental study, were integrated using the Seurat integration pipeline. The main NSC lineage was extracted via DBSCAN with eps=0.65 on UMAP coordinates and integrated with the supplemental data to identify neuronal clusters. DBSCAN was used again to identify the main component, resulting in our SVZ NSC reference lineage. Cellcycle scoring was carried out following the scanpy '180209_cell_cycle' example notebook with the there-supplied genes. Filtering for 1:1 orthologs we scored 51 G2M- and 42 S-phase genes. We set a G2M-score cutoff at 0.1 to determine cycling activity, which was consistent with expression of known cellcycle markers including MKI67, TOP2A, and UBE2C (not shown).

To generate an NSC lineage pseudotime, the PC2-lowest cell was chosen as the root for a diffusion map computed over PC1-3, and a branchless diffusion pseudotime[17] was computed over two diffusion components.

NSC Lineage QAD State Assignment And Pseudotime-predictive QAD Geneset

We identified QAD cell types through their frequency in pseudotime by fitting a Gaussian KDE over the noncycling NSC lineage pseudotime and finding density peaks using argrelextrema from scipy.stats[18]. Pseudotime 0-0.282 denotes Quiescence (0-0.141 as dormant astrocytic stages), 0.282-0.676 denotes Activation, and >0.676 denotes Differentiation.

To capture QAD cell states across datasets, genes were prefiltered by binning cells into 3333 equal-frequency pseudotime bins, excluding genes not reaching a summed expression threshold of 100 lognorm units or those not exceeding 40% mean counts per QAD state. Recursive feature elimination with a RandomForestClassifier on a 3-fold cross-validated 70/30 split reduced the feature set to 3333 genes. Then, 500 permutations of selecting 500 genes and training a RandomForestClassifier were performed, using the kneedle algorithm[19] to select pseudotime-predictive genes from ranked feature importances. Ribosomal genes were eliminated, and state-enriched genes were selected, taking up to 100 genes from each state, resulting in 242 genes assigned to QAD states based on maximum expression. GO-term enrichment was carried out using the enrichr class from gseapy[20] with expressed genes as background.

QAD Stages In Human Brain Development

Human brain development scRNA-seq datasets were retrieved from the meta-atlas compiled by [21] and reduced to 1:1 human-mouse orthologs. Samples with <300 cells were excluded and QAD-stages determined by maximum AUCell score. NSC lineage cell types were identified and the mean proportion of QAD-stages per timepoint calculated. QAD-stages were further compared to 'Type.v2' cell type labels from the metadata.

Human Cortical Organoids Processing and Lineage Pseudotime Assignment

Four HBOs were sequenced by 10X, distributing tumor and healthy FACS-sorted populations by lane. Fastq files were processed with Cellranger v6.0.0. Organoid-hashtags were counted by CITE-seq-count[22], assigning cells based on a 1.5-fold threshold of the most-frequent to second

most-frequent hashtag. Cells with >500 genes, >2000 UMIs, and <20% mitochondrial transcripts were retained. Healthy and malignant cells were separated using inferCNV[23] with 10X brain nuc-seq cells as a reference. inferCNV was run on genes with a mean lognorm expression value >0.25. Cells clustered by their 10X lane, and a Gaussian mixture model distinguished healthy and malignant cells using CNV calls from chromosomes 7, 8, 10, and 16. Lane- and CNV-concordant cells were retained for downstream analysis. The human NSC lineage was annotated by integration and DBSCAN-isolated healthy organoid cells were reclustered in a human NSC-lineage UMAP. We identified and excluded 847 cycling cells and derived a lineage diffusion pseudotime as above.

ptalign for Pseudotime Alignment

The ptalign program requires a query counts table, a reference counts table, a reference pseudotime mapping, and a set of trajectory genes. Query cells are placed along the reference pseudotime based on their gene expression correlation with trajectory genes. Reference cells are binned along pseudotime, mean expression per bin is calculated, and Pearson correlations are computed between query cells and pseudotime-binned references to represent a pseudotime similarity profile. Correlation scores from all cells are summarized in a correlation matrix, which is normalized and scaled. *ptalign* uses the supplied reference counts and reference pseudotime to compute a reference-reference correlation matrix and train a basic 3-layer multi-layer perceptron (MLP) network to predict the known reference pseudotime from the similarity profiles in the supplied matrix. A 5-fold cross-validated grid search optimizes MLP hyperparameters. Query cell pseudotimes are predicted by the trained network from input similarity profiles, with cell state inference based on reference pseudotime cutoffs. The quality of an assigned pseudotime is determined via DTW of the pseudotime-binned reference and an equally binned query. Counts are log-normalized and Pearson correlations computed for all combinations of reference and query bins. A matrix traceback is computed by dynamic programming to determine a path of maximal correlation through the DTW matrix. *ptalign* performance is estimated by comparing the length and average correlation along DTW traceback. These metrics are compared to reference-query matrices computed according to equally sized and equivalently expressed permuted genesets to determine an empirical p-value.

Human GBM PDX and PDA QAD States and Aligned Pseudotimes

Six 384-well plates of sorted T6 PDX tumor cells were prepared, two with SmartSeq3 and four with SmartSeq2. Reads were trimmed and mapped to the Ensembl 102 human and mouse genomes using STAR v2.5.3a. Cells were assigned to human, mouse, or QC-fail if they passed based on aligment rate and a human read ratio >1.3. The 1,176 QC-passing T6 Wnt-reporter cells were integrated using the Seurat pipeline, and cycling cells called. Pseudotime alignment was performed with default parameters, and QAD cell states assigned. This process was repeated for T6 PDA cells. Wnt activity in PDX cells was determined by FACS sorting relative to a reporter-positive control by index sorting. For PDA we sorted by Wnt activity into separate 10X lanes.

TCF-Lef SVZ Dataset

Five 384-well plates of sorted mouse brain populations from SVZ or OB were prepared using the SmartSeq3 protocol. Reads were trimmed with trim_galore[24] and mapped to the mm10 mouse genome using STAR v2.5.3a[25], then processed with a custom HTSeq count[26] script. Cell counts were QC-processed, log-transformed, and the NSC lineage was isolated by DBSCAN in UMAP space. Cycling cells were removed to produce a non-cycling lineage pseudotime. Pseudotime alignment was performed with default parameters, and QAD cell states were assigned using pseudotime cutoffs. Non-cycling lineage diffusion pseudotime and ptalign pseudotimes were compared by Pearson correlation per replicate to benchmark ptalign. This process was repeated for the HBO NSC lineage and pseudotime. Wnt activity in index-sorted PDX cells and TCF-Lef reporter SVZ reference lineage cells was assessed by fluorescence readouts relative to a reporter-positive reference gate.

Aligned Pseudotimes for Published External GBMs Datasets

We retrieved published primary GBM single-cell RNA-seq counts tables, listed in Table S1. Datasets were processed into an annotated counts table and subset to human-mouse 1:1 orthologs. All 66 datasets were merged and GBMs with >30% mitochondrial reads or <631 UMIs (corresponding to the smallest cell in the SVZ reference) were excluded. Tumor samples with fewer than 500 cells were also excluded, leaving 55. Counts were log-normalized per sample. Malignant cells were identified using inferCNV with a healthy CNV reference of 300 cells from our healthy HBO dataset. CNV genes were determined by comparing expression levels in healthy HBOs, our SVZ dataset, and GBM samples. Nonmalignant cell types were identified in UMAP space, and microglia, immune cells, and oligodendrocytes were excluded as in [27]. Cells with a Pearson correlation <0.4 to each sample's mean CNV calls were excluded, as well as tumors with <400 malignant cells, following method outlined in [27]. Cycling cells were excluded as described above and pseudotime alignment and QAD assignment were carried out for each tumor sample individually.

ptalign Pseudotime Coherence vs Conventional Trajectory Algorithms

For each of CytoTrace[28], Monocle3[29], and Palantir[30], pseudotimes for the 51-GBM cohort samples were determined according to the basic example in the respective documentation. For Monocle3 and Palantir, which require a root cell, the lowest cell in the ptalign pseudotime was chosen. These pseudotimes were compared to ptalign pseudotimes by pseudotime coherence. Per sample, a 10-component PCA was computed and cell's pairwise Euclidean distances determined. As conventional pseudotimes always span [0-1], we used rank-distances to represent pseudotime distance. These were compared to PCA distances by Pearson correlation, with the method-based differences in coherence assessed by paired t-test.

ptalign Permutation Benchmark in Non-brain Tissues

The ptalign permutation model was benchmarked against non-brain tissue tumors from [31]. Annotated malignant cells were isolated from colon ('Data_Lee2020_Colorectal'), breast ('Data_Qian2020_Breast') and lung ('Data_Kim2020_Lung') datasets. Samples with >500 cells were retained, cycling cells identified, and reduced to 1:1 human-mouse orthologs. ptalign was run per sample with default parameters for 100 permutations, with the p-values recorded.

Reproducing Genes2Genes Results on IBF Dataset

We reproduced the healthy-vs-disease comparison shown in Figure 5 of the Genes2Genes publication[32]. The datasets used are available from the Genes2Genes zenodo repository: 10.5281/zenodo.11182400. Gene were subset to human-mouse 1:1 orthologs and cycling cells excluded as above. We fit a banchless diffusion pseudotime through the healthy UMAP embedding, as described above, then split this lineage into 3 coherent leiden clusters for which we called predictive genes using the recursive approach described above, resulting in a 241-gene geneset. Then we ran ptalign with these genes and otherwise default parameters to arrive at an aligned pseudotime for cells from the diseased IBF dataset. The Genes2Genes authors determine that the diseased trajectory deviates in the late pseudotime, so we subset early, middle, and late pseudotime increments and computed the area under smoothed spline curves representing pseudotime gene expression for each pseudotime increment using the simpson function from scipy.integrate. We compute the area difference by taking the area under the absolute difference between healthy and diseased expression curves, and dividing it by the maximum coordinates along both healthy and diseased splines. We computed this ratio separately for each pseudotime increment. In Genes2Genes, EMT is enriched among genes deviating in late pseudotime, so we calculated the slope of the area difference ratio across pseudotime increments to identify those genes where the expression deviation is increasing (positive slope). We then conducted GSEA on genes ranked by this slope.

An GBM-derived QAD Geneset

We compared expression in GBM QAD stages with >20 cells to healthy SVZ QAD-expression. Genes seen in >80% of tumors were filtered by mean QAD-maximum lognorm expression. We computed normalized ranks of each gene by expression strength per state per tumor, selecting genes with >60% overrepresented ranking in a single state. These genes were compared to their state expression in the SVZ reference, again selecting by 60% enrichment in a given QAD-stage. DEseq log fold-changes in QAD-pseudobulks were used to take up to 100 genes per state, resulting in a 271-gene signature comprising 100 Q-, 71 A-, and 100 D-genes. A 92-gene cycling gene set was additionally derived by LFC>2.

QAD State Association with Tumor Clones by CNV

Clones were identified using hierarchical clustering on inferCNV-predicted CNV values. A linkage matrix was computed for each tumor and the first three splits used to define clones per tumor, reducing them to three or four putative clones which were further screened for CNV differences. CNV events >1.15 were considered gains and <0.85 losses. Tumors with fewer than 100 CNV events per cell were excluded. The ratio of CNV events in daughter clones was computed, and tumors where clones differed by <10% were excluded. For each of the remaining clones, we took the ratio of the average number of CNV events per cell per clone and compared to the value at the parent node. A z-score threshold of 0.5 identified clones with diverging CNV, and we assessed expression divergence in these clones by Pearson correlation.

GBM Microarrays and Clinical Data Curation

We collected microarray and clinical data from the TCGA-GBM cohort and Wu *et al*[33]. TCGA clinical metadata was obtained from the TCGA portal (https://portal.gdc.cancer.gov/) and merged using case_id fields. Recurrent GBMs were excluded. We curated TCGA-GBM data from Agilent 244K Custom Gene Expression arrays (https://portal.gdc.cancer.gov/legacy-archive/search/f), creating a new annotation file by aligning probes to the non-redundant nucleotide database (https://ftp.ncbi.nlm.nih.gov/blast/db/FASTA/nt.gz) with annotation by mygene v1.8. Background correction and normalization by LOESS-smoothing were performed, retaining only successfully annotated probes. Probes were summarized into gene sets, and low-quality arrays were excluded based on zero-count probes. Wu et al.'s data were processed in parallel, and survival reported in months was transformed to days.

GBMs QAD Scoring and Survival Comparison

RNA bulk and microarray counts for GBMs were scored for SVZ-QAD (Fig. 1) and GBM-QAD (Fig. 2; Fig. S6) genesets using the R GSVA package[34]. For survival analysis we right-censored by patient death and considered survival intervals up to the 95th percentile. A Cox proportional hazards (lifelines[35]) regression was carried out on the continuous QAD- and cellcycle GSVA-scores individually when accounting for patient sex and age, then adjusting for multiple testing.

Methylation Datasets Acquisition and RNA States Prediction

We obtained TCGA-GBM samples processed by EPIC450k array and matched them to their RNA counterparts. Methylation values from the Wu et al cohort were retrieved from GSE121722. We filtered compiled probe data to 'cg' probes not on sex chromosomes, with MAF<0.01. Variable methylation sites were computed by the kneedle algorithm, selecting a cutoff in the cumulative distribution of variance over mean, then used in PCA.

Intra-tumoral distances were compared in the Wu et al tumor cohort, with pairwise euclidean distances in methylation and RNA space computed for all tumor pairs, then compared by Pearson correlation. Elasticnet regression predicted GSVA QAD scores from methylation data in a grid-search paradigm. After a 66/33 train-test split, variable features were selected by taking the 5000 probes with the largest zscore in the methylation PC2-4 loadings, as well as 2000 probes with the highest correlation in QAD scores, resulting in a 10.259 probe feature set for training. Methylation betas at this probeset were normalized and scaled using the StandardScaler and used in a GridSearchCV with 5-fold cross-validation to optimize the mean squared error and determine the optimal l1_ratio, alpha, and fit_intercept parameters. The grid-search selected parameters were used to train models on the training data and evaluated on the test data.

Dysregulated Genes in GBM vs SVZ by EMD

We first select a representative 12,581 gene set expressed in both tumor and healthy contexts by requiring genes to be expressed above a threshold in 1% of cells per sample, for at least 10% of samples. Then we preprocess each sample and fit splines to represent pseudotime expression using the skfda package[36]. We define a grid over pseudotime at intervals of 0.05. For each sample, we group cells into bins along the pseudotime grid, then filter bins containing <20 cells. We define 5 basis splines over the range [0-1] with a smoothing parameter using L2 regularization

over the second derivative. We fit splines per gene on the expression mean per bin per sample, clipping negative values at 0. We store the resulting spline coordinates as well as area-normalized curves using the simpson function from scipy.integrate. For each gene we combine spline values from healthy samples and take their average, then area-normalize as above. We use the scipy.stats wasserstein distance (EMD) implementation to compute the distance of the averaged healthy curve to each of the area-normalized genes in tumor samples. Unexpressed genes receive a wasserstein distance of 1. We further derive the v-SVZ Q-D expression bias from area-normalized splines by defining Q- and D-intervals in the pseudotime grid, then computing the ratio of Q-area over summed Q- and D-areas.

We identify recurrently dysregulated genes by their mean GBM-SVZ wasserstein distance across GBMs. To avoid noise introduced by area-normalization, we focus on genes in the upper 50% of expression levels as inferred by spline area, with secondary filtering by expression levels in v-SVZ. Genes which are lost in >50% of tumors and ptalign genes are also excluded, leaving 5,415 genes for consideration. We rank genes by mean EMD as indicated above, and use the kneedle algorithm to identify the inflection point. 169 genes fall beyond this point, comprising the dysregulated gene set. We use the gseapy enrichr library to compute GO enrichments in this group, using non-dysregulated genes as background.

Genes from major signaling pathways are identified based on membership in the GO-BP 2023 ontology downloaded using gseapy. By retaining GO terms containing 'Wnt', 'BMP', 'Notch', or 'Smoothened' and not containing ‘Negative’, we pool genes associated to each pathway and count their occurrence by pathway. Genes are associated to the pathway in whose terms they most frequently appear in, with a lower bound of 50% enrichment. As ‘Wnt’ contains the most terms in GO, we additionally exclude genes which occur only in Wnt-associated terms but are seen <3 times overall, leaving 158 gene-pathway associations: 62 Wnt, 47 Notch, 31 BMP, and 18 Smoothened (SHH).

Biomarkers and Targets in Q- vs D-biased GBMs

GBMs are clustered by QAD- and cycling-proportions using ward linkage, and the first split used to separate into two groups of QA- and AD-enriched tumors. We compute pairwise group EMDs similar as above, additionally accounting for within-group consistency of EMD values. Thus, spline values along the pseudotime grid are collated for all tumors within a group, then EMDs computed for each group member to the group mean. Finally, group-mean EMDs between QA and AD tumors are computed. We then filter genes where the within-group EMD is >0.1, leaving 6,852 genes for consideration.

For selected biomarkers STMN1 and SOX11, and dysregulated genes KLF4 and ZFP36, we assayed bulk RNA expression and methylation levels by group in our TCGA cohort (see above). For methylation, we used the PC2-3 embedding of variable sites as above, to identify tumors where methylation aligned with dominant RNA stages: deriving 6 Q-enriched and 8 D-enriched tumors corresponding to QA- and AD-groups, respectively. Then we polled methylation probes covering our genes of interest, and plotted the methylation beta per sample, highlighting those probes where the absolute methylation difference between groups was >0.15. For RNA expression, we used differences in Q and D GSVA scores in the bulk TCGA and Wu et al cohort,

as above. Tumors with an absolute score difference >0.6 were assigned to QA- and AD-groups, comprising 29 and 41 tumors, respectively, enabling expression comparisons by group.

SFRP1 and NOTUM Overexpression Datasets

Sorted cells from T6 SFRP1- and NOTUM-overexpressing PDXs were sequenced, trimmed, and mapped as above. Cycling cells were removed, and pseudotime alignment was performed for QAD assignments. SFRP1 samples underwent pseudobulk DEseq analysis, followed by GSEA for enrichment among expression differences. Expression differences in the single NOTUM-overexpressing replicate were quantified using pseudobulk LFC to Wnt-reporter SmartSeq3 replicates. T6 SFRP1-overexpressing and Wnt-reporter cells injected into HBOs were sequenced on the 10X platform. Libraries were processed, and inferCNV distinguished malignant and healthy cell populations. Pseudotime alignment was carried out for tumor cells from each organoid. Healthy cells from SFRP1 and Wnt-reporter conditions were isolated, and cell types were identified by marker expression in a leiden clustering. Genotypic comparison of healthy cell type expression was performed by averaging expression between pseudobulk replicates per cell type.

WGBS Data Processing and SVZ DMR Readout

WGBS libraries were prepared in triplicate from PDX samples as in [12]. A combined human-mouse reference genome was generated[37] to map reads from mouse and human cells using Bismark v0.2033[38] with Bowtie2 v2.3.5.134[39]. Paired reads were trimmed by trim_galore, and single-end reads individually mapped to the combined human-mouse reference with Bismark, setting –q -N 1 -D 30 -R 3 -p 6 with --non_directional. PCR duplicates were removed using deduplicate_bismark, and mate-pairs recombined by merging deduplicated R1 and R2 BAMs with samtools merge. Finally, we ran the bismark_methylation_extractor tool with --bedGraph to quantify DNA methylation and counted CpG coverage using coverage2cytosine. CpG coverages were parsed and mouse and human methylation fractions per CpG determined separately. v-SVZ cell type DMRs from [40] were mapped to the human genome using liftOver, allowing up to 20% deviation in coordinate. DMRs with a genotype methylation difference >1 st.dev from the mean were considered differentially methylated.

Spatial Alignment & Preprocessing

For every ROI, Resolve Biosciences provided both 3D transcript positions and identities and a 2D DAPI image, which first needed to be integrated with our 3D confocal DAPI images. Resolve captures data in a tiled manner within every ROI; since they still had some stitching issues, every tile was separately aligned to the corresponding confocal image along the xy axes, using a homography obtained by matching SIFT features between the 2D DAPI image and a max-projection of the 3D DAPI image. Different angles of the slide in both microscopes were corrected by finding the angle of the slide plane in both modalities and rotating the transcript positions accordingly. The plane was fitted to the center of mass of the DAPI intensity along the z-axis for the 3D image, and to the tiled mean z position for the transcripts. Finally, a further shift along the z-axis was added such that the share of transcripts within segmented nuclei was maximized, using the segmentation described below.

Segmentation

The 3D DAPI images were segmented into nuclei with mesmer[41], using the default pretrained model in the nuclear mode. Our images have a resolution of 0.142 microns per pixel, but to stay closer to their training data we used 0.3 microns per pixel as the parameter for the segmentation. Segmentation was performed separately for every z-layer of the image, and afterwards stitched across the z-axis with a modified version of the intersection over union based approach used in [42]. Segmentation of the ROIs into different brain regions was performed by hand.

The transcripts were then segmented with Baysor[43]. Baysor first clusters the transcripts by their neighborhood; we chose to demand 21 clusters as this was the lowest number where each major cell type had at least one clear corresponding transcript cluster. Afterwards, it segments the transcripts into cells and background noise. Where transcripts intersected directly with segmented nuclei, this was added as the prior segmentation with confidence 0.98. The scale parameter was set to 2 microns, and we chose a minimum of 3 transcripts per cell. We excluded the transcript mCherry since it appeared to contain a lot of technical artefacts.

The parameters for Baysor were chosen to encourage over-segmentation rather than under-segmentation to properly resolve dense areas like tumors. To finally arrive at real cells, we assigned the Baysor cells to their nearest segmented nuclei, taking care to only combine Baysor cells that correspond to the same cell type. Prior to this, we consolidated the Baysor clusters to get rid of cases where multiple clusters corresponded to the same cell type. The assignment was done iteratively, first assigning Baysor cells that have a clear overlap with nuclei, and afterwards assigning the remainder to their closest compatible nucleus, starting with the Baysor cells with the most transcripts. Transcripts that Baysor marked as noise, and Baysor cells that could not be assigned to a segmented nucleus, were dropped.

Spatial Data Analysis

Cell types for mouse cells (>60% mouse transcripts) were obtained by associating Baysor clusters with cell types. To assign human cells, we marked the transcripts that are enriched in each state (e.g. Q+ transcripts are enriched in Q). Cells with less than 20% Q+ or A+, or 10% D+ transcripts were marked as generic human. Cells with at least 0.6 times as much Q+ as A+ or D+ were assigned Q, with at least 0.6 times as much D+ as Q+ or A+ were assigned D, and the remainder was assigned A.

Neighborhood enrichment was calculated using squidpy[44], using a radius of 20 microns to construct the neighborhood graph. The permutations were performed on the respective brain regions, combining all relevant regions from different ROIs. Squidpy reports the enrichment as number of actual neighbors compared to number of expected neighbors, normalized by the standard error of the expected number. This was multiplied by the square root of the number of cells in the permutation to obtain z-scores in terms of the standard deviation, since this is a measure of the effect size that does not scale with the overall number of cells that entered the computation.

Quantification and Statistical Analysis

Statistical analyses were performed in python using the scipy module. All p-values were calculated using a two-sided test, unless specified otherwise. Multiple testing correction was carried out using the python statsmodels library. Box plots each span the 25th and 75th percentile while the center lines indicate the median and the whiskers represent the absolute range. The handling of outliers is indicated in the respective figure legends.

References

1. Okita, K. *et al.* A more efficient method to generate integration-free human iPS cells. *Nat Methods* **8**, 409–412 (2011).
2. Ferrer-Vaquer, A. *et al.* A sensitive and bright single-cell resolution live imaging reporter of Wnt/ß-catenin signaling in the mouse. *BMC Dev Biol* **10**, 121 (2010).
3. Tiscornia, G., Singer, O. & Verma, I. M. Production and purification of lentiviral vectors. *Nat Protoc* **1**, 241–245 (2006).
4. The ORFeome Collaboration. The ORFeome Collaboration: a genome-scale human ORF-clone resource. *Nat Methods* **13**, 191–192 (2016).
5. Lancaster, M. A. *et al.* Guided self-organization and cortical plate formation in human brain organoids. *Nat Biotechnol* **35**, 659–666 (2017).
6. Lancaster, M. A. & Knoblich, J. A. Generation of cerebral organoids from human pluripotent stem cells. *Nat Protoc* **9**, 2329–2340 (2014).
7. Lancaster, M. A. *et al.* Cerebral organoids model human brain development and microcephaly. *Nature* **501**, 373–379 (2013).
8. Kalamakis, G. *et al.* Quiescence Modulates Stem Cell Maintenance and Regenerative Capacity in the Aging Brain. *Cell* **176**, 1407-1419.e14 (2019).
9. Stoeckius, M. *et al.* Cell Hashing with barcoded antibodies enables multiplexing and doublet detection for single cell genomics. *Genome Biol* **19**, 224 (2018).
10. Buenrostro, J. D. *et al.* Single-cell chromatin accessibility reveals principles of regulatory variation. *Nature* **523**, 486–490 (2015).
11. Picelli, S. *et al.* Full-length RNA-seq from single cells using Smart-seq2. *Nat Protoc* **9**, 171–181 (2014).
12. Cerrizuela, S. *et al.* High-throughput scNMT protocol for multiomics profiling of single cells from mouse brain and pancreatic organoids. *STAR Protocols* **3**, 101555 (2022).
13. Kremer, L. P. M. *et al.* High throughput screening of novel AAV capsids identifies variants for transduction of adult NSCs within the subventricular zone. *Molecular Therapy - Methods & Clinical Development* **23**, 33–50 (2021).
14. Carvajal Ibañez, D. *et al.* Interferon regulates neural stem cell function at all ages by orchestrating mTOR and cell cycle. *EMBO Mol Med* **15**, e16434 (2023).
15. Cebrian-Silla, A. *et al.* Single-cell analysis of the ventricular-subventricular zone reveals signatures of dorsal and ventral adult neurogenesis. *eLife* **10**, e67436 (2021).
16. Cunningham, F. *et al.* Ensembl 2022. *Nucleic Acids Research* **50**, D988–D995 (2022).
17. Haghverdi, L., Büttner, M., Wolf, F. A., Buettner, F. & Theis, F. J. Diffusion pseudotime robustly reconstructs lineage branching. *Nat Methods* **13**, 845–848 (2016).
18. Virtanen, P. *et al.* SciPy 1.0: fundamental algorithms for scientific computing in Python. *Nat Methods* **17**, 261–272 (2020).
19. Satopaa, V., Albrecht, J., Irwin, D. & Raghavan, B. Finding a 'Kneedle' in a Haystack: Detecting Knee Points in System Behavior. in *2011 31st International Conference on Distributed Computing Systems Workshops* 166–171 (IEEE, Minneapolis, MN, USA, 2011). doi:10.1109/ICDCSW.2011.20.
20. Fang, Z., Liu, X. & Peltz, G. GSEApy: a comprehensive package for performing gene set enrichment analysis in Python. *Bioinformatics* **39**, btac757 (2023).
21. Nano, P. R. *et al.* A Meta-Atlas of the Developing Human Cortex Identifies Modules Driving Cell Subtype Specification. Preprint at https://doi.org/10.1101/2023.09.12.557406 (2023).

22. Stoeckius, M. *et al.* Simultaneous epitope and transcriptome measurement in single cells. *Nat Methods* **14**, 865–868 (2017).

23. inferCNV of the Trinity CTAT Project. (2024).

24. TrimGalore.

25. Dobin, A. *et al.* STAR: ultrafast universal RNA-seq aligner. *Bioinformatics* **29**, 15–21 (2013).

26. Anders, S., Pyl, P. T. & Huber, W. HTSeq—a Python framework to work with high-throughput sequencing data. *Bioinformatics* **31**, 166–169 (2015).

27. Neftel, C. *et al.* An Integrative Model of Cellular States, Plasticity, and Genetics for Glioblastoma. *Cell* **178**, 835-849.e21 (2019).

28. Gulati, G. S. *et al.* Single-cell transcriptional diversity is a hallmark of developmental potential. (2020).

29. Cao, J. *et al.* The single-cell transcriptional landscape of mammalian organogenesis. *Nature* **566**, 496–502 (2019).

30. Setty, M. *et al.* Characterization of cell fate probabilities in single-cell data with Palantir. *Nat Biotechnol* **37**, 451–460 (2019).

31. Gavish, A. *et al.* Hallmarks of transcriptional intratumour heterogeneity across a thousand tumours. *Nature* **618**, 598–606 (2023).

32. Sumanaweera, D. *et al.* Gene-level alignment of single-cell trajectories. *Nat Methods* **22**, 68–81 (2025).

33. Wu, Y. *et al.* Glioblastoma epigenome profiling identifies SOX10 as a master regulator of molecular tumour subtype. *Nat Commun* **11**, 6434 (2020).

34. Hänzelmann, S., Castelo, R. & Guinney, J. GSVA: gene set variation analysis for microarray and RNA-Seq data. *BMC Bioinformatics* **14**, 7 (2013).

35. Davidson-Pilon, C. lifelines: survival analysis in Python. *JOSS* **4**, 1317 (2019).

36. Ramos-Carreño, C., Torrecilla, J. L., Carbajo-Berrocal, M., Marcos, P. & Suárez, A. **scikit-fda** : A *Python* Package for Functional Data Analysis. *J. Stat. Soft.* **109**, (2024).

37. Callari, M. *et al.* Computational approach to discriminate human and mouse sequences in patient-derived tumour xenografts. *BMC Genomics* **19**, 19 (2018).

38. Krueger, F. & Andrews, S. R. Bismark: a flexible aligner and methylation caller for Bisulfite-Seq applications. *Bioinformatics* **27**, 1571–1572 (2011).

39. Langmead, B., Trapnell, C., Pop, M. & Salzberg, S. L. Ultrafast and memory-efficient alignment of short DNA sequences to the human genome. *Genome Biol* **10**, R25 (2009).

40. Kremer, L. P. *et al.* Single-cell triple-omics uncovers DNA methylation as key feature of stemness in the healthy and ischemic adult brain. *bioRxiv* (2022) doi:10.1101/2022.07.13.499860.

41. Greenwald, N. F. *et al.* Whole-cell segmentation of tissue images with human-level performance using large-scale data annotation and deep learning. *Nat Biotechnol* **40**, 555–565 (2022).

42. Stringer, C., Wang, T., Michaelos, M. & Pachitariu, M. Cellpose: a generalist algorithm for cellular segmentation. *Nat Methods* **18**, 100–106 (2021).

43. Petukhov, V. *et al.* Cell segmentation in imaging-based spatial transcriptomics. *Nat Biotechnol* **40**, 345–354 (2022).

44. Palla, G. *et al.* Squidpy: a scalable framework for spatial omics analysis. *Nat Methods* **19**, 171–178 (2022).

Data and Code Availability

The *ptalign* software will be made available on GitHub prior to publication. Jupyter notebooks detailing the analyses and figures in this study are deposited in Zenodo: https://doi.org/10.5281/zenodo.14968415. Newly generated SmartSeq3 datasets of the mouse v-SVZ NSCs lineage are available from GEO with accession GSE240676, along with processed tumor PDX and PDA single-cell RNA-sequencing and WGBS datasets. Raw tumor data subject to DPA are submitted to EGA. Spatial transcriptomics data we generated are submitted to Zenodo under https://zenodo.org/deposit/8186500. Samples and metadata from the TGCA-GBM cohort are available through the NCI GDC Data Portal (https://portal.gdc.cancer.gov/). Bulk GBM data from Wu *et al*. was received in personal communication. All data supporting the findings of this study are available from the corresponding author upon reasonable request.

Acknowledgements

We gratefully acknowledge the following DKFZ core facilities for their support and expert assistance: Center for Preclinical Research, Small Animal Imaging Center, Genomics and Proteomics (Microarray Unit and Sequencing Open Lab), Single Cell Open Lab, Flow Cytometry and Light Microscopy. We are thankful to the Division of Biostatistics for statistical support. We further thank the following members of the Division of Molecular Neurobiology for their technical support: Santiago Cerrizuela, Lukas Kremer, Irene Lois Bermejo, Hadil El-Sammak, Andres Sanz Morejon, Damian Carvajal Ibanez, Jooa Hooli, Susanne Kleber, Katrin Volk, Kathrin Menzner, Mohammad Al-Shukairi, Heike Abendroth, Aylin Korkmaz and all the members of our group and the members of the Somatic Evolution and Early Detection group for continuously providing critical feedback on the project as well as the manuscript. 7TGC plasmid was a gift from Roel Nusse; RKRR-P2A plasmid was a gift from Edward Green. OK was funded by the Helmholtz International Graduate School for Cancer Research. This work was supported by the German Cancer Research Center (DKFZ), European Research Council (ERC; REBUILDCNS and PEPS, no. 101071786), and the German Research Foundation (DFG; SFB1324). Last but most important, we are grateful to patients and their families for their generous donations to biomedical research.

Author Contributions

LCF developed a computational tool for analysis of activation state architecture of tumors and conducted computational analysis; conceptualized, designed, and analyzed experiments and interpreted results; and wrote the manuscript. OK developed experimental protocols, conceptualized, designed and performed experiments and interpreted results; and wrote the manuscript. VW performed the analysis of spatial transcriptomics data; DPD performed mathematical modelling; VA, MB, KCZ, NS, JT, JB, NGP contributed to the development of the experimental protocols and supported experiments. XM and HL provided human brain organoids; AS and CO contributed to the analysis of TCGA data; CRW provided GBM samples and clinical data; AMC supervised mathematical modeling; SA and AG supervised computational analysis. AMV conceived and directed the project, conceptualized and designed experiments, interpreted results, and wrote the manuscript.

Declaration of Interests

LCF, OK and AMV have filed a patent application.